Elena Romero Adam

Trabajo de fin de Máster

ALIGNMENT OF THE ATLAS INNER DETECTOR TRACKING SYSTEM

Contents

1 Introduction

During 2010 and 2011 the Large Hadron Collider (LHC) [1] has produced proton-proton collisions at an unprecedented centre-of-mass energy of 7 TeV. These collisions have been recorded with ATLAS [2], a general-purpose experiment designed to search for new physics phenomena and to test the Standard Model (SM) [3] at these high energies.

The efficient and precise reconstruction of charged particle tracks is a basic aspect of high-energy physics experiments. In order to achieve its scientific goals, ATLAS is equipped with several sub-detectors: a very precise Inner Detector (ID) tracking system [4], the calorimeter system [2] and the muon spectrometer [2].

The ID consists of three subsystems: the Pixel detector, the Semiconductor Tracker (SCT) and the Transition Radiation Tracker (TRT). After the assembly of the ID, the position of the individual detector elements is known with less precision than their intrinsic resolution. Therefore, in order to fully exploit their excellent spatial resolution, an alignment procedure has to be applied to accurately determine their position and orientation.

The baseline goal of the ID alignment is to determine the position and orientation of the active detector components such that the track parameter resolutions are not significantly degraded (no more than 20%) with respect to those derived with perfect knowledge of the detector geometry. In addition, the alignment should correct for systematic effects that could bias the track-parameter determination.

This document summarizes the track-based alignment of the ID using LHC proton-proton data collected at a centre-of-mass energy of 7 TeV and cosmic-ray data recorded between LHC collisions.

In section 2 a brief description of the LHC and its experiments and, after that, a more detailed description of the ATLAS experiment is given. In section 3 one can find an overview of the Inner Detector with its subdetectors. Section 4 is devoted to the Alignment of the ID, giving a detailed explanation of its motivations, the data used, the procedure followed, the results obtained and a summary of its history over the years. Section 5 is dedicated to the ID Alignment Monitoring and it shows some of its newest relevant histograms. And to finalize, in section 6 the conclusions are presented.

2 The Large Hadron Collider

In 1952 the Conseil Européen pour la Recherche Nucléaire (CERN) was created by 11 European countries. Two years later, this Council established the laboratory that was constructed in the border between France and Switzerland. Today it is one of the world's leading particle physics facilities.

The largest international scientific project in the world nowadays is the LHC, which includes a hadron accelerator, four huge detectors at its four collision points and a Computing Grid project which maintains the data storage and analysis infrastructure. The LHC, located at CERN near Geneva (Switzerland), is the first accelerator that will explore extensively the TeV scale. It is expected to provide answers to questions like the origin of the particle masses through the electroweak breaking symmetry mechanism. Moreover it will also look for experimental evidence of new and exciting theories such as Supersymmetry or Extra Dimensions.

The LHC will produce two proton beams in opposite directions with an energy up to 7 TeV each (i.e. centre of mass collision energies of up to 14 TeV) and with a design luminosity[1] of 10^{34} $cm^{-2}s^{-1}$. The LHC will also collide heavy ions, in particular lead nuclei, up to 5.5 TeV per nucleon pair, at a design luminosity of 10^{27} cm^{-2} s^{-1}.

In order to accelerate the proton beams, the existing CERN accelerator complex is used. The last injection heads towards the LHC ring, which is, nowadays, the longest hadronic accelerator ever built with its 27 km long circumference, laying 100 m below ground. Each beam has an internal structure arranged in bunches separated in space which condense up to 1.1×10^{11} protons. At nominal operation, collisions will occur at a rate of 40 MHz (i.e. one collision every 25ns).

Finally, in the LHC ring there are four detectors placed at the LHC collision points. These detectors are:

- **A Toroidal LHC ApparatuS (ATLAS)** [2]: It is a general purpose experiment for high luminosity (up to 10^{34} $cm^{-2}s^{-1}$) which will perform high precision measurements on SM parameters and the Higgs boson search. It is the largest LHC detector with 44 x 25 m^2 and weighting 7000 tons. It has two magnets: one 2T solenoid for the inner detector, and a toroid which generates up to 6 T/m for the muon spectrometer.
- **Compact Muon Solenoid (CMS)** [5]: It is the other general purpose experiment for high luminosity (up to 10^{34} cm^{-2} s^{-1}) and it has the same discovery potential as ATLAS although its hardware and software design is different. It is smaller than ATLAS (21 x 15 m^2) although heavier with 12500 tons and it can generate a unique non-linear magnetic field up to 4 T.
- **Large Hadron Collider beauty (LHCb)** [6]: This experiment is a low luminosity experiment (up to 10^{32} cm^{-2} s^{-1}) for measuring the parameters of CP violation in the interactions of B-hadrons. The LHCb detector is a single arm spectrometer stretching for 20 metres along the beam pipe, with its subdetectors stacked behind each other.
- **A Large Ion Collider Experiment (ALICE)** [7]: This experiment is focused on heavy ions and quark-gluon plasma studies. It will operate at a peak luminosity of 10^{27} cm^{-2} s^{-1} for nominal Pb-Pb ion operation.

And it also has three smaller experiments:

- **Total cross section based on the Optical TheorEM (TOTEM)** [8]: The aim of this experiment is to measure total cross sections, elastic scatterings at small angles and diffractive processes at the LHC at low luminosities (up to 2×10^{28} cm^{-2} s^{-1}). It shares intersection point with CMS.
- **Large Hadron Collider forward (LHCf)** [9]: It is a special purpose experiment for low luminosity (up to 2×10^{28} cm^{-2} s^{-1}) which will study neutral pions produced in the forward region of collisions. It shares the same cavern with ATLAS and it consists of two detectors, installed at 140 m on either side of the intersection point.
- **Monopole and Exotics Detector at the LHC (MoEDAL)** [13]: The prime motivation of MoEDAL is to directly search for the Magnetic Monopole or Dyon and other highly ionizing Stable (or pseudo-stable) Massive Particles (SMPs) at the LHC. It is installed around the intersection region of the LHCb detector, in the VELO (VErtex LOcator) cavern.

---

[1] The luminosity $\mathcal{L}$ is an accelerator parameter which depends on the number of particles per bunch in the two colliding beams, N_1 and N_2, on the bunch crossing frequency f and on the bunch area. Thus, assuming a Gaussian transverse particle bunch profile, the $\mathcal{L}$ is defined as:

$$\mathcal{L} = \frac{1}{4\pi}\frac{N_1 N_2}{\sigma_x \sigma_y} f N_b$$

where N_b is the number of bunches and σ_x and σ_y are the Gaussian widths in the horizontal and vertical plane of the bunch respectively.

The last piece of the LHC project is its computing model which has the aim of building and maintaining a distributed data storage and analysis infrastructure for the entire community that uses the huge amount of data that the LHC is producing based on Grid technologies [10].

2.1 The ATLAS detector

ATLAS [2] is a general-purpose experiment designed to realize the main physics goals of the LHC, namely searches for the Higgs boson and for physics beyond the SM. The formal proposal for ATLAS was prepared in 1994 and 10 years later the detector installation in the cavern began. The ATLAS collaboration is quite large with more than 2500 physicists scattered around the world.

The ATLAS detector is nominally forward-backward symmetric with respect to the interaction point. It has cylindrical shape (4π coverage) with several layers of subdetectors. It is 44 m long and 25 m high. The closest system to the beam pipe is the tracker or Inner Detector. It operates embedded in a 2 T magnetic field, generated by a thin superconducting solenoid surrounding the ID cavity, and consists of silicon-based subdetectors and drift tubes. This ensures a robust pattern recognition, momentum and charge determination, precise primary and secondary vertex reconstruction, as well as particle identification capability. Outside the solenoid the calorimeters are located. First, the electromagnetic calorimeter [2] uses liquid argon as an ionization medium, with the absorbers arranged in an accordion geometry. It allows the identification and measurement of electrons and photons. Surrounding the latter is the hadronic calorimeter [2] that uses a scintillating tile technology allowing to measure hadronic jets[2] and helping to determine the missing energy. Outside the calorimeters, ATLAS has a large muon spectrometer [2], which performs the measurement of muon momenta. It rests inside an air core toroidal magnetic field that is generated by three large superconducting toroids (one barrel and two end-caps) arranged with an eight-fold azimuthal symmetry around the calorimeters. This generates a strong bending power in a large volume within a light and open structure, thereby minimising multiple-scattering effects and allowing to achieve excellent muon momentum resolution with three layers of high precision tracking chambers. The muon spectrometer is the outermost part of ATLAS therefore it defines the overall dimensions of the detector (see Figure 2.1).

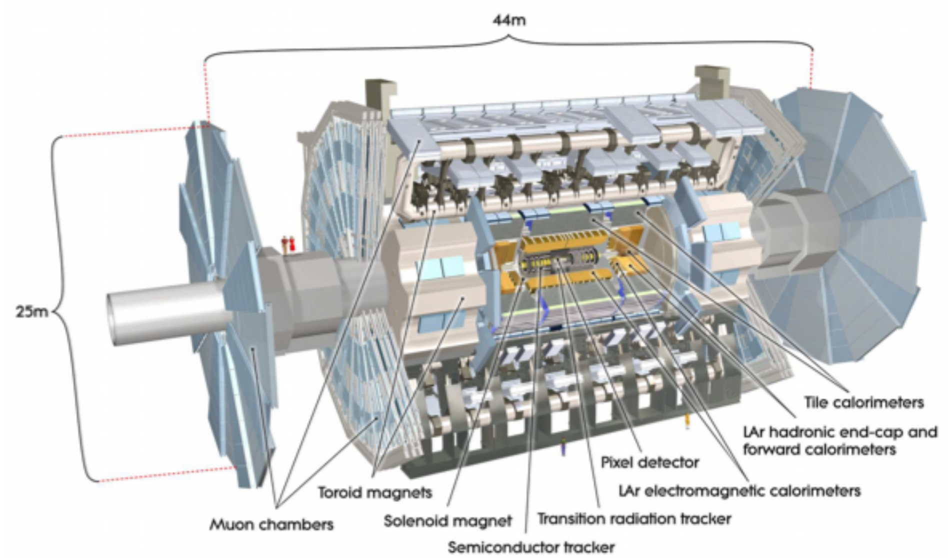

[2] A jet is a narrow cone of particles produced by the hadronization of the quark or gluon.

Figure 2.1: *The ATLAS detector with all its subdetectors labelled. Moreover, several human figures, barely visible, are included for a scale reference.*

Another important part of the ATLAS detector is its trigger system. The LHC proton bunches will collide at a frequency of 40 MHz, i.e. every 25ns, and at the design luminosity of 10^{34} cm^{-2} s^{-1}. On average about 23 inelastic proton-proton collisions will be produced at each bunch crossing. Therefore, the trigger system needs to efficiently reject a large rate of background events and select the potentially interesting ones with high efficiency. To deal with this amount of data that these collisions will generate the ATLAS trigger [11] is based on three levels of online event selection: L1, L2 and the Event Filter. Each trigger level refines the event selection done by the previous level, applying new criteria.

2.1.1 Coordinate system

Before going any further it is useful to briefly summarise the coordinate system and nomenclature used to describe the ATLAS detector and the particles emerging from the p-p collisions. The nominal interaction point[3] is defined as the origin of the coordinate system, while the beam direction defines the z-axis, and the x-y plane is transverse to the beam direction. The positive x-axis is defined as pointing from the interaction point to the centre of the LHC ring and the positive y-axis is defined as pointing upwards. The side-A of the detector is defined as that with positive z and side-C is that with negative z. The azimuthal angle ϕ is measured as usual around the beam axis, and the polar angle θ is the angle from the beam axis. The pseudorapidity is defined as $\eta = -\ln \tan(\theta/2)$. The transverse momentum p_T, the transverse energy E_T, and the missing transverse energy E_T^{miss} are defined in the x-y plane unless stated otherwise. The distance ΔR in the pseudorapidity-azimuthal angle space is defined as $\Delta R = \sqrt{\Delta\eta^2 + \Delta\phi^2}$.

3 Inner Detector

The ID is the closest detector to the interaction point in ATLAS and its task is to reconstruct trajectories of charged particles. Its design provides hermetic and robust pattern recognition, excellent momentum resolution and both primary and secondary vertex measurements for charged tracks (the later being needed to identify e.g. B-mesons and converted photons) above a given p_T threshold (nominally 0.5 GeV) and within the pseudorapidity range $|\eta| < 2.5$. It also provides electron identification over $|\eta| < 2.0$ and for a wide range of energies (between 0.5 GeV and 150 GeV).

[3] Nominal Interaction Point (IP): design position of the IP. Real or physics IP: position where the particles actually collide (also called primary vertex)

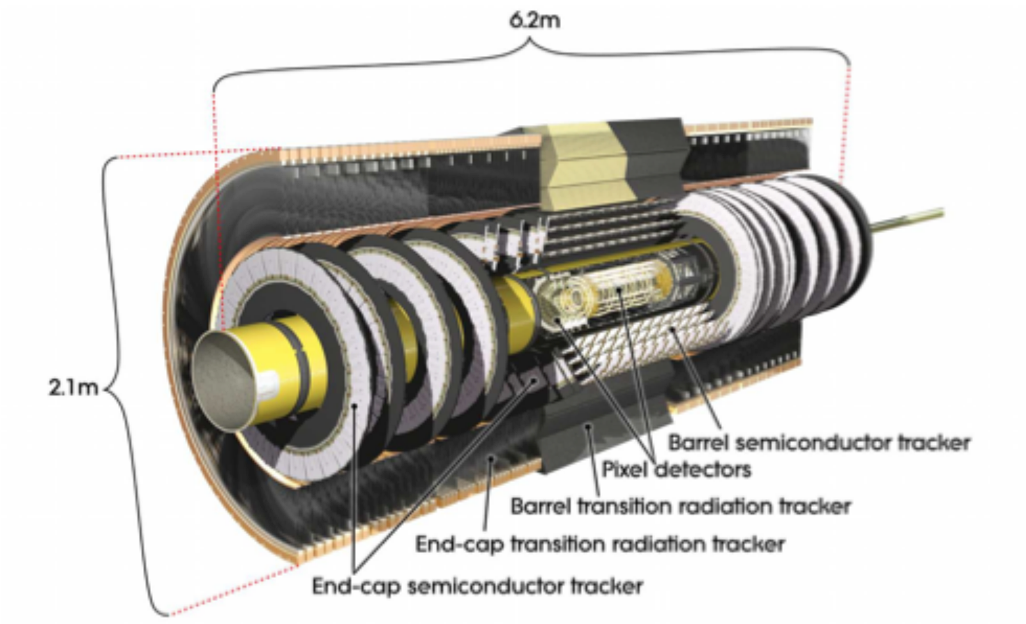

Figure 3.1: ATLAS Inner Detector. Comprising the pixel detector, the SCT and the TRT.

The ID layout, which is shown in Figure 3.1, consists of three different subdetectors based on different technologies:

- A silicon pixel detector, referred simply as the Pixel detector, provides generally three 3-dimensional spacepoints per track (two measuring coordinates per hit), allowing spacepoint formation.
- A silicon strip detector, also known as SCT, surrounds the pixel detector and provides at least four 3-dimensional spacepoints, this detector gives one measuring coordinate per hit, but each module has two sides which can be combined in order to build a spacepoint.
- A straw tracker, called TRT, surrounds the other two subsystems and provides about 36 straw hits in the plane transverse to the beam pipe.

All three subsystems are divided into a barrel part and two end-caps. The barrel parts consist of several layers of sensors whilst the end-caps are composed of a series of discs or wheels of sensors.

The pixel and strip detectors are based on silicon as a detection medium. These detectors provide a very good granularity and very precise position measurements but they require a lot of material in the form of support structures and cooling pipes. This material has a negative effect on the performance of the tracker. This was one of the main reasons to minimize the material used to build the outermost layer of the ID, being the TRT made of gas-filled straws.

Moreover, these subdetectors are installed in a solenoid magnet, which provides a magnetic field of 2 T, making possible to measure the momentum of the charged particles, by measuring the curvature of the tracks in the ID. Figure 3.2 shows a plan view of a quarter-section of the ATLAS ID where the exact position and dimensions of each barrel layer and discs of each subdetector are labelled. Also the solenoid and the ID services and patch-panels are shown in that figure. Moreover, the ID is contained within a cylindrical envelope of length ± 3512 mm and radius 1150 mm, within the solenoid which can also be seen in the figure.

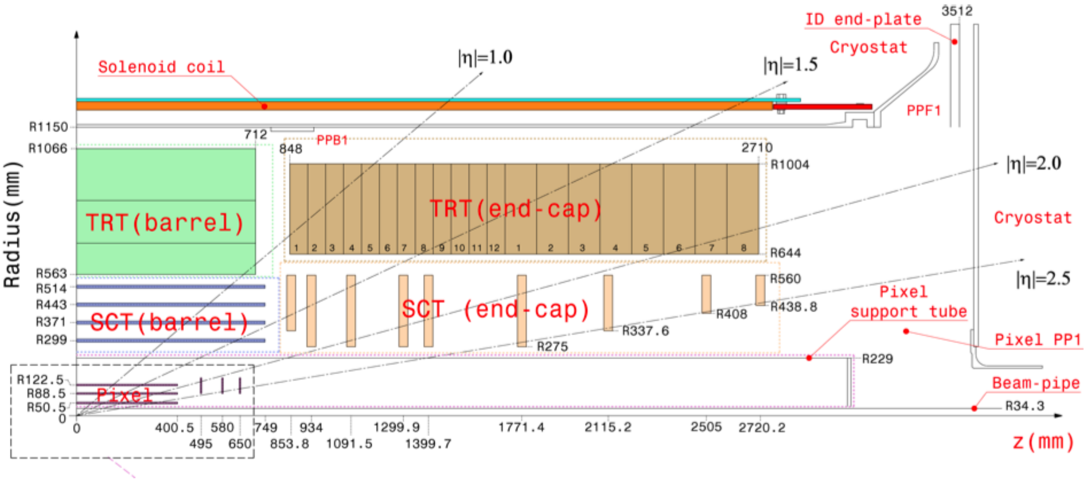

Figure 3.2: *Plan view of a quarter-section of the ATLAS ID showing the exact position of each part of each subdetector as well as their envelopes, patch-panels, services and the solenoid.*

Finally, figures 3.3 and 3.4 show nominal positions of each barrel layer and end-cap disc in the radial and transverse plane, respectively. The knowledge of these nominal positions is very important, as these are the starting positions for the track-based alignment algorithms.

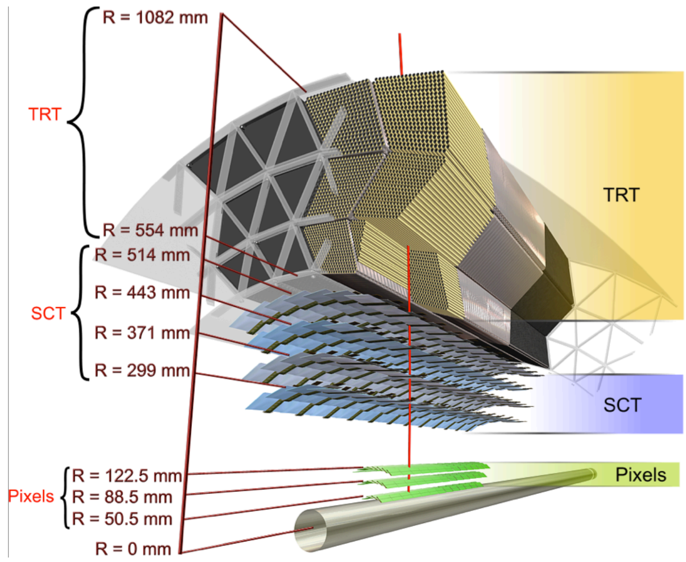

Figure 3.3: *Drawing showing the position of the barrel detectors and structural elements.*

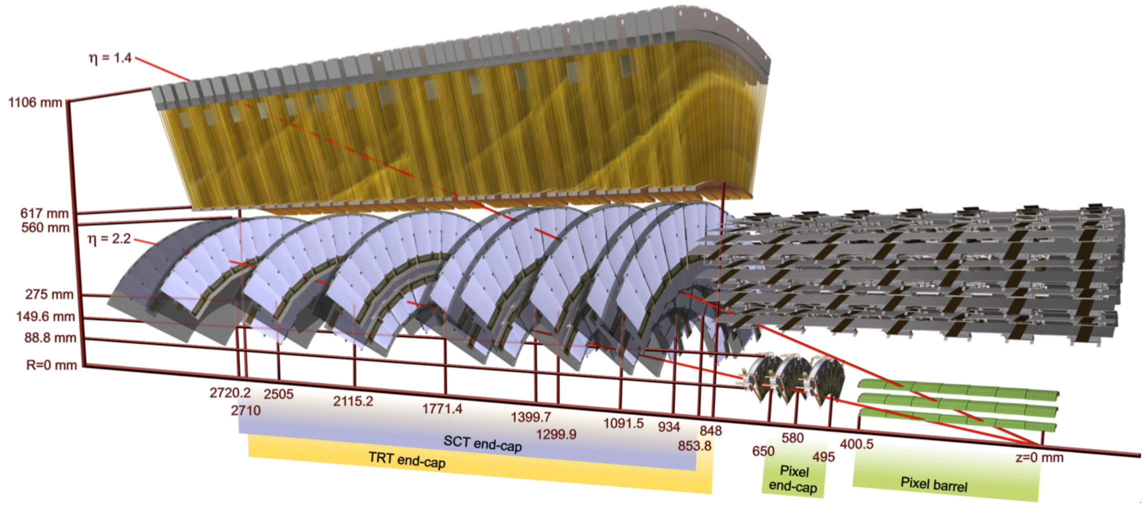

Figure 3.4: *Drawing showing the position of the barrel and end-cap structural elements. Tracks will traverse different detector layers depending on their pseudorapidity.*

3.1 The silicon Pixel detector

The Pixel detector [11] is designed very close to the collision point to provide a high tracking precision and to find relatively long-lived particles such as b-quarks and τ-leptons. The Pixel subdetector is based on silicon pixel technology and it is arranged in three cylindrical barrels and three discs on each side of the central barrel with a coverage of $|\eta| < 2.5$ as Figures 3.3 and 3.4 show. Each of these structures consists on 1744 identical pixel modules. Barrel modules are arranged along staves which are carbon-fibre structures (13 modules per stave). These staves are lying parallel to the beam axis but they are inclined by an azimuthal angle of 20º around the long axis, which means that the superposition of two modules in each layer is about 200 μm as can be seen in figure 3.5. Moreover, staves are grouped in half-shells and then these structures form the barrel layers. Finally, each end-cap disc contains 24 modules (divided in 8 sectors) per side as shown on figure 3.6. Table 3.1 gives the barrel layers and discs positions together with the number of modules per structure.

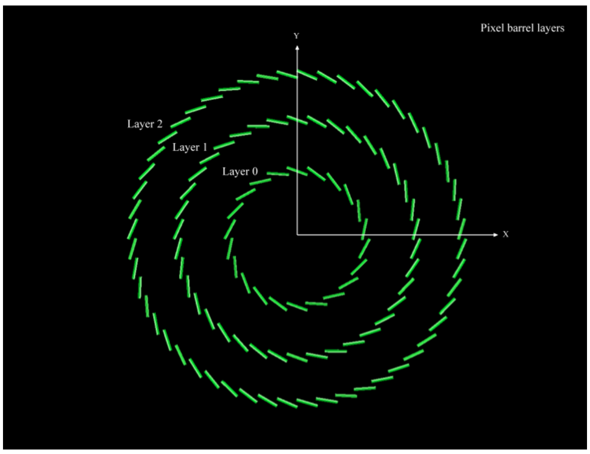

Figure 3.5: *Schematic transverse view of the Pixel detector where its layers can be observed as well as the module tilts.*

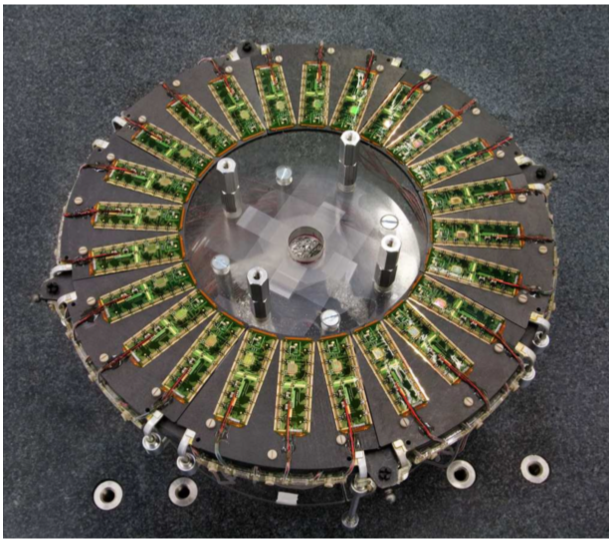

Figure 3.6: *Photograph of a pixel end-cap disc.*

Structure	Layer/Disc	Radius/Z (mm)	Staves/Sectors	Modules	Pixels
Barrel	0	50.5	22	286	$13.2 \cdot 10^6$
	1	88.5	38	494	$22.8 \cdot 10^6$
	2	122.5	52	676	$31.2 \cdot 10^6$
End-Cap	0	± 495	8	48	$2.2 \cdot 10^6$
	1	± 580	8	48	$2.2 \cdot 10^6$
	2	± 650	8	48	$2.2 \cdot 10^6$
All				1744	$80.4 \cdot 10^6$

Table 3.1: *Summary table of the Pixel detector for each of the barrel layers and end-cap discs.*

The pixel elements size is 50 × 400 μm^2. The intrinsic resolution of the pixel modules is 10 μm in the rϕ (module local x) direction and 115 μm in the module local y direction (the local y direction is parallel to the LHC beam-pipe for barrel modules and radial for end-cap ones) with a direct 2D readout. This system is designed to provide a very high granularity with 80.4 million channels.

3.2 The silicon microstrip detector

The silicon microstrip detector [11], also referred as SemiConductor Tracker (SCT), surrounds the pixel detector and it uses also silicon planar sensors.

The detector consists on four cylindrical layers in the barrel region and nine end-cap discs on each side. The barrel layers and discs distances are shown in figures 3.3 and 3.4 whilst the exact numbers are listed in table 3.2. The SCT has 4088 modules in total. The barrel modules are mounted in staves and then these structures are mounted with a tilt angle of 11^o in the barrel layers, which translates in an overlap of 4 mm between modules. The geometry configuration of the end-caps is quite complex as each disc has a different number and type of SCT end-cap modules as can be read in table 3.3.

Layer	Radius (mm)	Modules	Area (m^2)		
0	300.0	12 × 32	6.26	Barrel length:	1.4934 m
1	373.0	12 × 40	7.82	Strip pitch:	80.0 μm
2	447.0	12 × 48	9.4	Total number of modules:	2112
3	520.0	12 × 56	10.96	Total area:	34.4 m^2
				Number of channels:	3244032

Table 3.2: *Summary of the SCT Barrel specifications.*

A SCT module consists on two silicon sensitive sensors which are based on strips that give 1-dimensional position measurements. Both SCT module sides are glued together back-to-back at a 40 mrad stereo angle. In the barrel, the module side parallel to beam pipe is called rϕ side and the other side is known as the stereo side.

The SCT has a single module topology design for the barrel region with a rectangular module type and three topologies for the end-caps having trapezoidal shapes, namely *outer*, *middle* and *inner* according to their position in the end-cap wheels. The strip pitch is 80μm in the barrel module, while in the end-cap modules, as they have a fan-out structure, the strip pitch is variable: from 54.53 μm to 90.34 μm, depending on the wafer position.

Disc	**Z (mm)**	**Radius (mm) [*Inner/Outer*]**	**Modules [I / M / O]**	Strip pitch [min/max] (*μm*)	
0	± 835.0	259 / 560	40 / 40 / 52	- *Inner:* 54.53 / 69.43	
1	± 925.0	336 / 560	- / 40 / 52	- *Middle:* 70.48 / 94.74	
2	± 1072.0	259 / 560	40 / 40 / 52	- *Outer:* 70.92 / 90.34	
3	± 1260.0	259 / 560	40 / 40 / 52	Types:	4
4	± 1460.0	259 / 560	40 / 40 / 52	Total number of mods:	1976
5	± 1695.0	259 / 560	40 / 40 / 52	Total area:	26.7 m^2
6	± 2135.0	336 / 560	- / 40 / 52	Number of channels:	3035136
7	± 2528.0	401 / 560	- / 40 / 52		
8	± 2788.0	440 / 560	- / - / 52		

Table 3.3: *Summary of the SCT end-caps specifications.*

The combination of two back-to-back side measurements allows to determine the position of the hits along the strips giving the SCT modules the capability for a 3-dimensional spacepoint reconstruction. Once a spacepoint is built, the intrinsic resolution of a whole SCT module is 17 μm in rϕ (direction across the strips) and 580 μm in z.

3.3 The TRT detector

The TRT [2] consists of about 300,000 proportional drift tubes (straws) of 4 mm of diameter each and a sensing wire in its centre. The straw tubes are grouped together in 176 modules arranged in 73 layers in 3 rings in the barrel region and 2 × 160 straw planes in 40 four-plane assembly units in the end-cap regions. The straws in the barrel part are arranged parallel to the beam axis, while in the end-caps the straws are radially oriented. The TRT straw tubes have a single hit resolution of 130 μm, but no measurement along the straw direction is given. The TRT gas mixture $Xe/CO_2/O_2$ (70%/27%/3%) provides an efficient X-ray absorption, a fast charge collection and a stable operation over a sufficient high-voltage range even at high particle rates. From the practical design point of view, it has been built to provide, in the barrel region on average 36 TRT hits for tracks coming from the interaction point. Figure 3.7 shows a photograph of one quarter of the barrel TRT during integration.

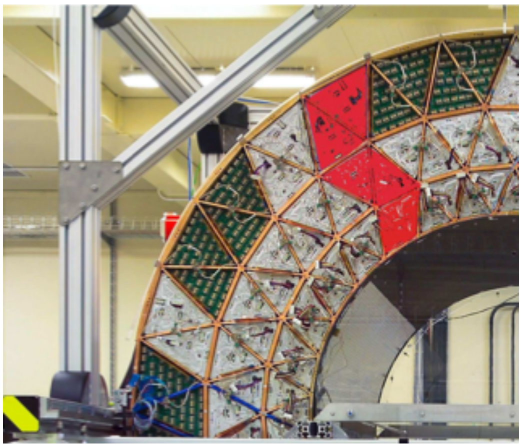

Figure 3.7: *Photograph of one quarter of the barrel TRT during integration.*

4 Alignment of the Inner Detector

4.1 Motivations: Why the alignment is needed?

The efficient and precise reconstruction of charged particle tracks is a basic aspect of high-energy physics experiments. For example, lepton reconstruction algorithms use Inner Detector tracks to reconstruct and calculate the lepton 4-momentum. Also vertex finders and b-tagging algorithms rely on tracks.

Any misalignment of the different detector elements will degrade the track measurements and therefore the lepton reconstruction, the b-tagging, etc. Furthermore, as these algorithms are used elsewhere in physics analysis, the alignment becomes crucial especially for SM precision measurements and new discoveries.

The ATLAS detector, and in particular its Inner Detector, has been built with high resolution tracking devices. But after the assembly of the ID, the position of the individual detector elements is known with less precision than their intrinsic resolution. Therefore, in order to fully exploit their excellent spatial resolution, an alignment procedure has to be applied to accurately determine their position and orientation.

The goal of the alignment is set such that the limited knowledge of the sensor location should not deteriorate the resolution of the track parameters by more than 20% with respect to the intrinsic tracker resolution [4]. This translates into a requirement on the precision of the positioning of the silicon devices, which has to be better than 10 μm. In addition, the alignment should correct for systematic effects that could bias the track-parameter determination.

4.2 Implementation of the Alignment Algorithm

The determination of the position and orientation of each active detector element is achieved via track-based alignment algorithms [11], the implementation of which will be presented in this section.

Each alignable structure has 6 basic degrees of freedom. These correspond to the 3 translations (T_x, T_y, T_z) that determine its position and 3 rotations (R_x, R_y, R_z) that designate its orientation. Internal module distortions may be parameterized and used, that may add extra degrees of freedom.

An alignable structure can range from a single silicon module or TRT wire, to a complete barrel layer or end-cap disk with many modules, or even an entire subdetector. Alignment of larger structures composed of multiple detector elements uses the ATLAS global reference frame (described in section 2.1.1). Alignment of the individual detector modules uses a local Cartesian right-handed reference frame with the origin in the geometrical centre of the object.

- In the Pixel and the SCT, the x and y-axes are in the detector plane with the x-axis pointing along the most precise measurement direction.
- In the TRT modules and wires the z-axis points along the wire. The x-axis is perpendicular to both the wire direction and the radial direction from the origin of the global frame to the straw centre.

In the case of individual detector modules, it is further possible to consider certain detector module deformations. For example, a silicon module may be modelled as a perfectly flat surface, or as a plane that may be twisted or bent. In the current implementation of the ID alignment procedure, pixel module distortions are used as surveyed during the assembly. The module distortion parameters are not recomputed during the alignment procedure.

In addition to the track-based alignment algorithms, the ID alignment can make use of several additional types of information. For example, it is possible to use the survey data obtained during the assembly of the detector. Online information from the Frequency Scanning Interferometry (FSI) system [11], an optical alignment system installed in the SCT, is also available, though not yet used.

Before explaining the track-based alignment algorithms it is worth it to explain which are the track parameters and what is a residual.

4.2.1 Track parameters

The trajectory of a charged particle, i.e. a track, in a uniform magnetic field (B) is a helix, which can be parameterized by a set of five parameters.

In the ATLAS software this helical trajectories are parameterized as five dimensional vectors with the following parameters:

$$\boldsymbol{\tau} = (d_0, z_0, \phi_0, \theta, q/p),$$

where d_0 is the transverse impact parameter which is the signed distance to the XY plane, and that sign is defined to be positive when the direction of the track is clockwise with respect to the origin and therefore flipping the direction will flip the sign of the impact parameter. Then, z_0 is the longitudinal impact parameter which is the z-coordinate of the perigee (in this case the perigee is the point of closest approach to the origin of the global frame), ϕ_0 is the azimuthal angle in the XY plane at the perigee, and θ is the polar angle, i.e. the angle with the z-axis. The fifth parameter is q/p which is the charge of the particle divided by its momentum. (The transverse momentum, p_T is computed as $p_T = p \sin\theta = 0.3qBr$). Figure 4.1 shows a representation of these parameters.

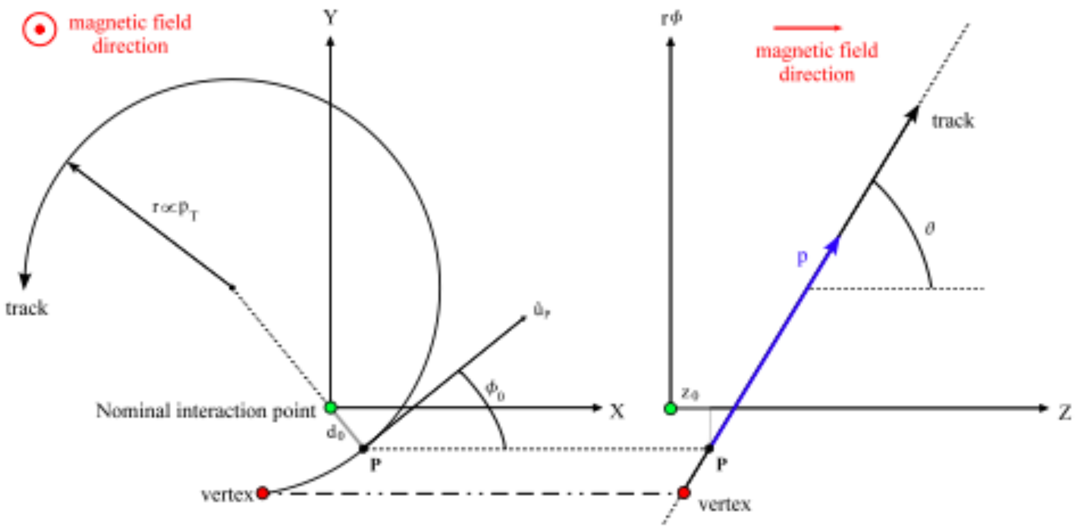

Figure 4.1: track parameters defined at the perigee, ***P****, computed with respect to the origin of the global frame.*

4.2.2 Residuals

For tracking, a residual is the distance between a hit (the detector measurement) and the intersection point of the extrapolated (or fitted) track in the sensor. More rigorously

$$\mathbf{r} \equiv \mathbf{m}(\mathbf{a}) - \mathbf{t}(\boldsymbol{\tau}),$$

where the vector **m** denotes the position of the hit and depends on the alignment parameters **a** = (T_x, T_y, T_z, R_x, R_y, R_z). And the vector **t** denotes a point on the extrapolated track and depends on the track parameters $\boldsymbol{\tau}$. A pixel hit always has two residuals r_x and r_y, while a hit on a plane of an SCT module has only one residual in the direction perpendicular to the strip coordinate.

In High Energy Physics (HEP) there are two residual concepts used for tracking and alignment purposes: "biased" and "unbiased" residuals (which are not frequently used in other fields).

- Biased residual: The track fit is performed with all the available hits which belong to this track, including the hit of the considered residual measurement.
- Unbiased residual: the reconstructed track does not include the data point under test, i.e. the hit on the surface where the residual is being calculated. This means that to calculate every unbiased residual on each measuring surface one has to refit the track every time removing the hit under test. Thus, computing time for unbiased residuals is larger than for biased residuals.

Residual distributions of a perfectly aligned detector are centred at zero and have a width corresponding to the resolution of the specific readout coordinate and detector type. For Pixel x-residuals this would be a width of 10 μm, for y-residuals 115 μm and for SCT residuals 17 μm. Consequently a necessary condition for a set of final alignment corrections is to produce centred and narrow residual distributions.

4.2.3 The Track-based Alignment Algorithms

Several track-based alignment algorithms have been implemented within the ATLAS software framework. All of them derive the alignment parameters **a** by minimizing the track residuals. For this purpose a χ^2 function is built from the residuals of all collected tracks as follows:

$$\chi^2 = \sum_{tracks} \boldsymbol{r}^T V^{-1} \boldsymbol{r}, \tag{1}$$

where $\mathbf{r} = \mathbf{r}(\boldsymbol{\tau}, \mathbf{a})$ is the vector of the track-hit residuals for a given track, which depends on the track parameters $\boldsymbol{\tau}$ and the alignment parameters $\mathbf{a}$. V represents the covariance matrix of the hit measurements (which may include the contribution from multiple Coulomb scattering). The χ^2 minimisation is done with respect to the alignment parameters **a.** The alignment parameter vector **a** contains all degrees of freedom being aligned. In general it will be a repetition of the basic vector $\mathbf{a} = (T_x, T_y, T_z, R_x, R_y, R_z)$ for every structure being aligned. The minimisation condition of the χ^2 with respect to **a** gives:

$$\frac{d\chi^2}{d\boldsymbol{a}} = 0 \longrightarrow 2\sum_{tracks} \left(\frac{dr}{d\boldsymbol{a}}\right)^T V^{-1}\boldsymbol{r} = 0. \tag{2}$$

The track-hit residuals are initially computed for an initial set of alignment parameters ($\mathbf{a}_0$) and track parameters ($\boldsymbol{\tau}_0$), thus giving an initial estimate: $\mathbf{r}_0 = \mathbf{r}(\boldsymbol{\tau}_0, \mathbf{a}_0)$. The essence of the Global χ^2 [11] algorithm is to minimise the χ^2 by fitting simultaneously all tracks and alignment parameters. Therefore, one obtains corrections ($\delta\boldsymbol{\tau}$ and $\delta\mathbf{a}$) to the initial parameters. The final solutions are thus:

$$\boldsymbol{\tau} = \boldsymbol{\tau}_0 + \delta\boldsymbol{\tau} \text{ and } \mathbf{a} = \mathbf{a}_0 + \delta\mathbf{a}.$$

The track and alignment parameter corrections enter in the Global χ^2 expressions via the Taylor's expansion of the residuals[4]. As the residual is a multivariate function, the expansion up to first order is given by the following expression:

$$\boldsymbol{r} = \boldsymbol{r}_0 + \frac{\partial r}{\partial \boldsymbol{\tau}}\delta\boldsymbol{\tau} + \frac{\partial r}{\partial \boldsymbol{a}}\delta\boldsymbol{a}. \tag{3}$$

If the initial estimates are far from the final solution, then several iterations are needed in order to calculate the full correction. This is a consequence of neglecting the higher order corrections. The iterations must carry on until convergence has been reached. This equation explicitly depends on both track and alignment parameters and as such cannot be used with an arbitrarily large number of input tracks. In order to solve the problem, the track parameter dependence may be folded in, yielding:

$$\boldsymbol{r} = \boldsymbol{r}_0 + \left(\frac{\partial r}{\partial \boldsymbol{\tau}}\frac{d\tau}{d\boldsymbol{a}} + \frac{\partial r}{\partial \boldsymbol{a}}\right)\delta\boldsymbol{a} = \boldsymbol{r}_0 + \frac{dr}{d\boldsymbol{a}}\,\delta\boldsymbol{a}. \tag{4}$$

After inserting Equation (4) into Equation (2) one obtains the following expression:

$$\left[\sum_{tracks}\left(\frac{dr}{d\boldsymbol{a}}\right)^T V^{-1}\left(\frac{dr}{d\boldsymbol{a}}\right)\right]\delta\boldsymbol{a} + \sum_{tracks}\left(\frac{dr}{d\boldsymbol{a}}\right)^T V^{-1}\boldsymbol{r}_0 = 0.$$

The alignment matrix and vector can then be defined as:

---

[4] In ATLAS, the alignment corrections and the track-hit residuals are given in the local reference frame of each module. Therefore the calculation of the residual derivatives is also performed in the same local reference frame.

$$\mathsf{M}_a = \sum_{tracks} \left(\frac{dr}{d\boldsymbol{a}}\right)^T V^{-1} \left(\frac{dr}{d\boldsymbol{a}}\right) \text{ and } \nu_a = \sum_{tracks} \left(\frac{dr}{d\boldsymbol{a}}\right)^T V^{-1} \boldsymbol{r}_0. \quad (5)$$

Alignment corrections are then computed as:

$$\delta a = -\mathsf{M}_a^{-1} \, \nu_a, \quad (7)$$

which represents a linear system with as may equations as alignment degrees of freedom to solve. Determining a solution to the alignment problem involves two steps:

1. Filling the Global χ^2 alignment matrix (M_a) and the alignment vector (ν_a) from all the reconstructed tracks considered for the alignment,
2. Solving the system of linear equations.

The size of the alignment matrix may vary by several orders of magnitude. A few tens of degrees of freedom are considered when aligning large structures like barrels and/or end-caps, and many thousands when aligning at module level. For the latter, the memory and CPU consumption are of concern.

In the case of the Global χ^2 algorithm the alignment matrix (M_a) is usually dense. This is because the Global χ^2 method correlates the alignable structures that participate in the reconstruction of the same track. The matrix may become highly dense when filled with cosmic-ray tracks, because these tracks correlate different detector regions than the collision tracks (which are pointing to the centre). If the alignment matrix is not sparse but it is small (which is the case when aligning few degrees of freedom), then inverting the matrix is not difficult. However, if the matrix is not sparse and its size is large, then solving the linear system in Equation (6) is quite challenging from the computational point of view. It has to be noted that the M_a^{-1} is the covariance matrix of the alignment corrections. So, by inverting the alignment matrix, one has direct access to the errors of the alignment parameters.

A very practical way of making the alignment matrix sparse is by performing a Local χ^2 alignment [12]. In this case, the correlation between alignable structures is discarded and the tracks are not refitted. Thus, in the Local χ^2 case, each structure is aligned locally with respect to the others. In the Local χ^2 approach the alignment matrix (M_a') and vector (ν'_a) from Equation (6) are reduced to:

$$\mathsf{M}'_a = \sum_{tracks} \left(\frac{\partial r}{\partial \boldsymbol{a}}\right)^T V^{-1} \left(\frac{\partial r}{\partial \boldsymbol{a}}\right) \quad \text{and} \quad \nu'_a = \sum_{tracks} \left(\frac{\partial r}{\partial \boldsymbol{a}}\right)^T V^{-1} \boldsymbol{r}_0$$

The crucial point in the Local χ^2 approach is that M_a' becomes block diagonal. Hence, the Local χ^2 method is less demanding in computer resources because the matrix inversion is much less CPU time consuming than the full Global χ^2 matrix, and the memory usage is also much smaller. On the other hand, in the Local χ^2 method, the correlation between alignable structures is just recovered by successive iterations, and more of those are needed to reach convergence.

Generally, two types of constraints can be applied to the ID alignment:

- Constraints on track parameters, such as beam spot, primary vertex, and invariant mass constraints.
- Constraints on alignment parameters such as the use of survey information, FSI, and mechanical constraints.

When using constraints, extra terms are added to the χ^2 of Equation (1). Consequently, additional contributions enter the calculation of M_a and

ν_a. In the alignment procedure presented here, the only constraint applied was one on the transverse impact parameter of tracks. All tracks associated to the primary interaction vertex were required to remain consistent with the reconstructed LHC luminous region. This requirement removes certain weak modes of the alignment solution affecting impact parameter resolution and vertexing performance. The weak modes are alignment solutions that leave the χ^2 almost invariant but may introduce biases in the track parameters. The combination of different track topologies (collision and cosmic-ray tracks) helps to trim some of the weak modes (for more information about week modes see section 4.2.5).

4.2.4 Alignment Levels and Degrees of Freedom

As explained before, the basic detector units (silicon modules for pixel and SCT and straw tubes for the TRT) have been assembled in larger structures as barrel layers and end-cap disks or wheels. These structures have then been assembled into full barrels and/or end-caps for each Subdetector. Misalignments may have been introduced at each level of the detector mechanical assembly. A variety of survey information for each assembly level also exists.

The detector alignment is performed in a sequence of several levels of different detector granularity, following the assembly hierarchy. First, the largest structures, subdetector barrels and end-caps, are aligned. These have the largest misalignments, but require the smallest number of hits-on-tracks to accurately determine their alignment. A second level of alignment treats barrel layers and en-cap disks or wheels as separate alignable objects. At this level, more structures, and consequently more degrees of freedom, are aligned. The final alignment level consists of the module-by-module (Pixel, SCT) or wire-by-wire (TRT) alignment. This third alignment level has the most degrees of freedom and requires the greatest statistics.

In each alignment level, the degrees of freedom that are considered depend on both the expected misalignments from mechanical assembly, and on the sensitivity of each degree of freedom to the input data. Each alignable structure has six spatial degrees of freedom but not all of them can be aligned with the same accuracy. In some cases, the sensitivity is very small (for example, there is no measurement of the hit position along the TRT wire). In addition, depending on the module location (barrel or end-cap), the sensitivity of the same degree of freedom may vary. Therefore, in the current alignment not all the possible degrees of freedom are aligned at each level. Table 4.1 summarizes the number of alignable structures in the three ID subdetectors for the three alignment levels and the aligned degrees of freedom.

Alignment level	Detector	Structures	degrees of freedom used	number
Level 1	Pixel: whole detector	1	All	6
	SCT: barrel and 2 end-caps	3	All	18
	TRT: barrel	1	All (except T_z)	5
	TRT: 2 end-caps	2	All	12
	Total	7		41
Level 2	Pixel barrel: half shells	6	All	36
	Pixel end-caps: disks	6	T_x, T_y, R_z	18
	SCT barrel: layers	4	All	24
	SCT end-caps: disks	18	T_x, T_y, R_z	54
	TRT barrel: modules	96	All (except T_z)	480
	TRT end-caps: wheels	80	T_x, T_y, R_z	240
	Total	210		852
Level 3	Pixel: barrel modules	1456	All (except T_z)	7280
	Pixel: end-cap modules	288	T_x, T_y, R_z	864
	SCT: barrel modules	2112	T_x, T_y, R_z	6336
	SCT: end-cap modules	1976	T_x, T_y, R_z	5928
	TRT: barrel wires	105088	T_ϕ, R_r	210176
	TRT: end-cap wires	245760	T_ϕ, R_z	491520
	Total	356680		722104

Table 4.1: Summary of the main alignment levels and the number of structures for each ATLAS ID Subdetector, as well as the detail of the degrees of freedom being aligned and the total number of degrees of freedom aligned. The nomenclature of the degrees of freedom used in the TRT level 3 alignment is described in Section 4.3.2. All degrees of freedom are given in the local reference frame.

When aligning the subdetector structures (level 1 in Table 4.1) one handles only 41 degrees of freedom. According to the in-situ mechanical survey, initial misalignments of the order of 1 mm could be expected between the three Inner Detector barrel structures. Also, according to the mechanical survey and assembly data, the expected misalignments at levels 2 and 3 are much smaller. The level 3 alignment uses 356,680 structures (silicon modules and TRT wires) and in total 722,104 degrees of freedom. This is the level where the position of each individual detector element is corrected with respect to its neighbours. The expected size of the alignment corrections at this level are on the order of tens of micrometres, as the individual modules were assembled or surveyed with that precision using coordinate-measuring machines. It is also interesting to mention that, in order to provide alignment corrections for each individual module, every module has to have enough hits. Empirically it was found that 100 hits on a module are enough to achieve a proper alignment.

It must be noted that the "local" alignment coordinates xyz for the level 1 and level 2 structures coincide with the ATLAS global coordinate frame XYZ.

An example of the different silicon alignable substructures of each alignment level can be seen in the figure 4.2.

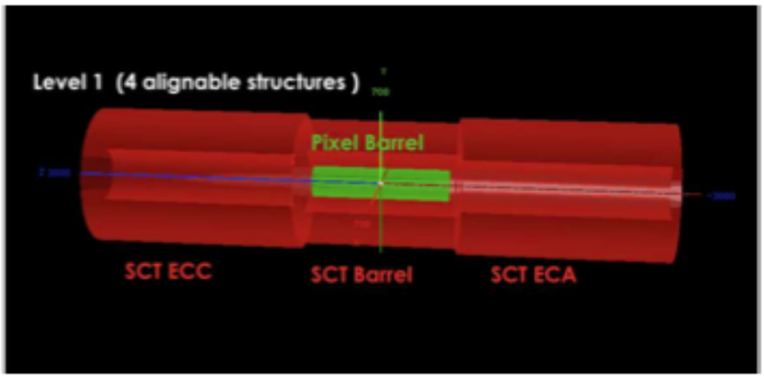

(a) *Alignment level 1 (4 alignable structures)*

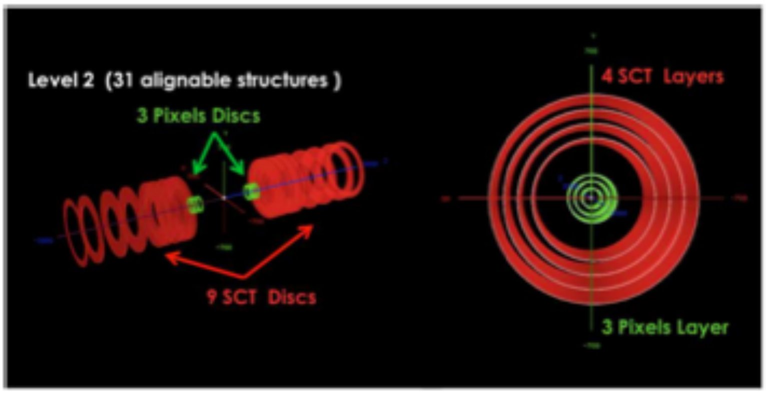

(b) *Alignment level 2 (31 alignable structures)*

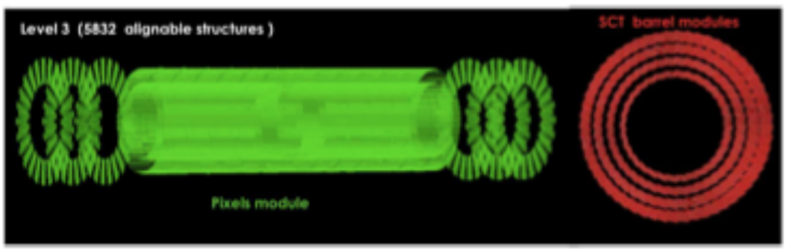

(c) *Alignment level 3 (5832 alignable modules)*

Figure 4.2: *Graphical models of the three main alignment levels. Figure (a) shows level 1 where the Pixel detector is represented with just one structure and the SCT is divided in three structures (the barrel and the two end-caps). Figure (b) shows level2, where the different barrel layers and end-cap discs are considered for both the Pixel and the SCT detectors. And Figure (c) shows level 3, which is the finest alignment level, where all the individual silicon modules are considered.*

4.2.5 Data Used in the Alignment Procedure

Two distinct track collections were used simultaneously as input for the alignment:

- Collision tracks: this sample consisted of a collection of high p_T and well isolated tracks. These tracks were selected from the LHC proton-proton collisions by the high-level trigger and put into a dedicated calibration stream.
- Cosmic-ray tracks: collected by the cosmic-ray triggers enabled between proton-proton collisions.

The online track selection of the collision tracks sample proceeds as follows: in those detector regions where the calorimeter energy is above a certain threshold, the online tracking algorithm reconstructs tracks using the Inner Detector raw data recorded in the same η - ϕ region of interest. The ID data are then stored in the collision tracks stream if there is at least one track that passes the p_T cut, and this track is found to be well isolated with respect to other tracks in the same region of interest. The actual values of the p_T and isolation ($\Delta R = \sqrt{\Delta\phi^2 + \Delta\eta^2}$) cuts are configurable and may depend on the luminosity and other operation conditions. Typically these are 9 GeV and 0.3 for the p_T and ΔR respectively. Moreover, a track quality cut was applied and 7 silicon hits were required for the collision tracks.

The cosmic-ray track sample consisted of tracks crossing the ID volume that were collected in parallel to the collision tracks. The cosmic-ray triggers were enabled during the LHC proton-proton physics runs but just during those periods without paired proton bunches passing through ATLAS. These cosmic-ray triggers are based upon calorimetry and muon system information. The recorded cosmic-ray tracks were stored in a separate calibration stream. As the cosmic-ray tracks are acquired in parallel with the collision tracks the detector geometry and operation conditions are exactly the same for both samples. The cosmic-ray tracks help the ID alignment in many ways, most importantly by introducing correlations between detector regions that are not correlated by collision tracks. Collision tracks do not cross opposite parts of the detector, whereas cosmic-ray tracks can cross the full barrel with modules in both the upper and lower barrel halves registering hits. Finally a track quality selection was applied and only those cosmic-ray tracks with more than 12 silicon hits, $p_T > 2$ GeV and $d_0 < 25$ cm were retained for the alignment.

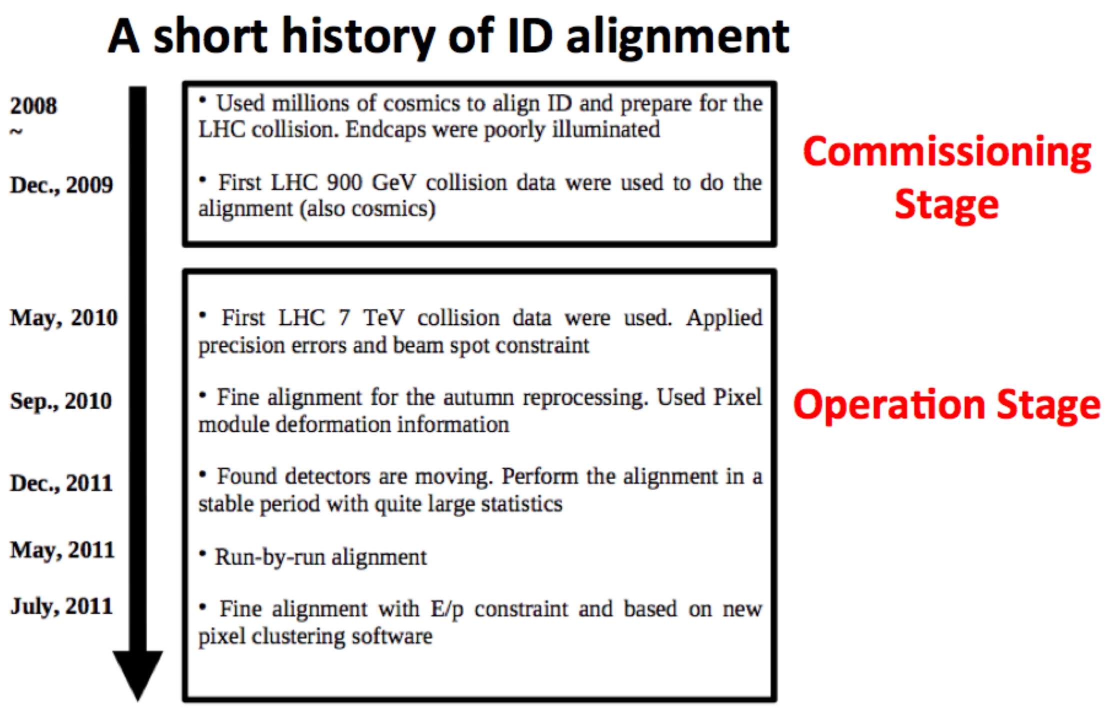

Figure 4.3: Alignment procedures and improvements since the beginning of the data taking.

It is interesting to comment the history of the ID alignment because it can give us a clue of the different steps that have been necessary to take in order to improve the corrections that are needed. In Figure 4.3 we can see a summary of these steps I am mentioning.

The first steps were taken in the commissioning stage. In the fall of 2008 and the summer of 2009, before the LHC had any collision beams, the whole ATLAS detector was accumulating cosmic-ray[5] data.

A schematic view of the ATLAS detector in the cavern, the rock and concrete formations above and surface area at ground level is shown in Figure 4.4. All the structures above ATLAS act as shielding that slows and stops the cosmic muons before reaching the detector. The two access shafts provide pathways for the muons with a minimal amount of material in the way. The access shafts and their different diameters result in a non-homogeneous illumination of the ATLAS detector with cosmic muons, leading to a much higher illumination of the barrel modules than for the end-cap modules where statistics were very low.

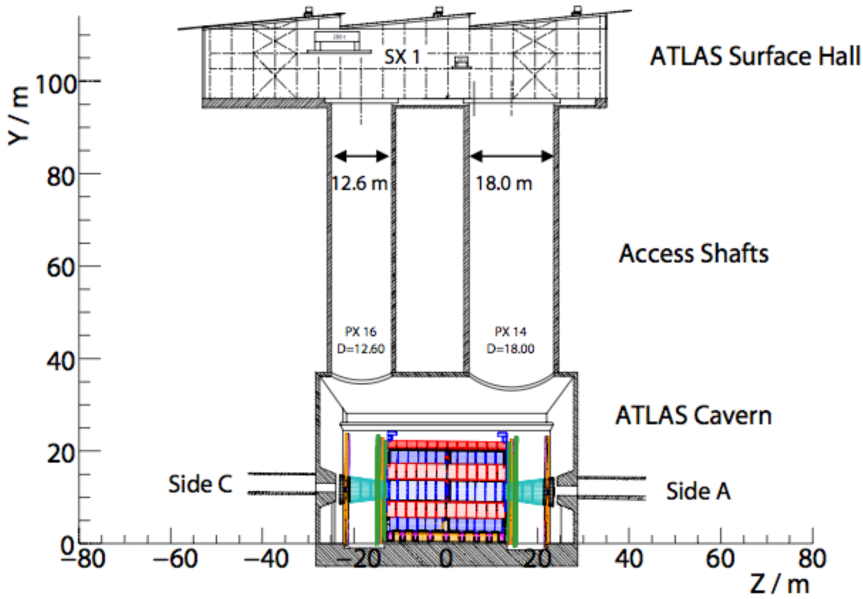

Figure 4.4: *Schematic drawing of the ATLAS detector in the cavern together with the access shafts through the rock, the concrete above the cavern and the surface building.*

It is also interesting to say that during these data taking periods a fraction of the runs was performed without magnetic field for test purposes and consistency checks. The tracks without magnetic field are not curved and are fitted as straight lines. These tracks act as a reference in the curvature reconstruction for tracks with infinite momentum. This provides valuable information for the alignment because it helps to correct misalignments that distort the curvature reconstruction.

Of course, this alignment with only cosmic tracks was necessary but no enough, so in December 2009, when the first collisions started to take place in the LHC, events at 900 GeV were used to improve the alignment and calibration of the different ATLAS subdetectors. This new period of the commissioning stage led to a significant improvement in the alignment of the end-caps of the Pixel detector, but especially in the end-cap C of the SCT ($\eta < -1.1$ region), due to the higher statistics in these regions, as it can be seen in Figure 4.5.

[5] The primary cosmic rays that hit the earth's atmosphere interact with the nuclei of the atmosphere and create secondary particles that in turn interact with other nuclei. A particle cascade called an air shower develops. The electrons, photons and muons of these showers reach the surface of the earth, but only the muons have the penetration power to also reach the ATLAS detector in the cavern below ground.

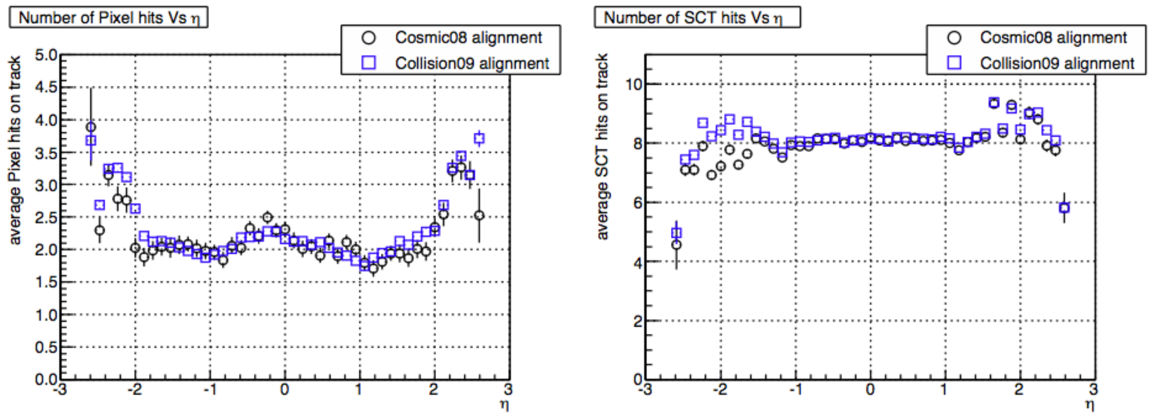

Figure 4.5: *Average number of Pixel and SCT hits as a function of η. Circles represent the Cosmic08 alignment while the squares represent the Collision09 alignment. Since different statistics have been used to construct each alignment set, plots are normalized to the number of tracks which have passed the quality cuts to allow comparisons.*

The next step in the ID alignment used the data collected during the LHC runs from March to July of 2010. This was the first time that events with 7 TeV of centre of mass energy were used for the ID alignment [14]. Depending on the alignment level, the actual size of the sample of tracks varied. In the alignment levels 1 and 2 (table 4.1) all the hits collected by the modules lying in the same alignable structure contribute to the hit statistics, which therefore accumulate fast. However, in order to collect enough hits per module for the level 3 alignment the full sample of 4.3 million and 300 thousand of collision and cosmic-ray were used. To check the quality of this alignment, an independent data set was needed. For this purpose a data set that comprises ~ 150,000 events collected from $\sqrt{s}$ = 7 TeV proton-proton collision runs taken between 29th July 2010 and 18th August 2010 was used.

The latter step will be the one presented in this work and a detailed explanation of this Alignment Procedure will be given in the next section. However, several important improvements have been made with the 2011 data and they will be briefly commented in this section.

Since May 2011, the luminosity of the LHC has increased to the point that there are enough statistics to perform the alignment run by run, allowing us to monitor the movements of the detector as a function of time. Figure 4.6 shows that, after hardware incidents, such as cooling failures or power cuts, the detector movements are of the order of less than 10 μm. Whereas, in between these periods little movements (< 1 μm) are observed, indicating that the detector is generally very stable.

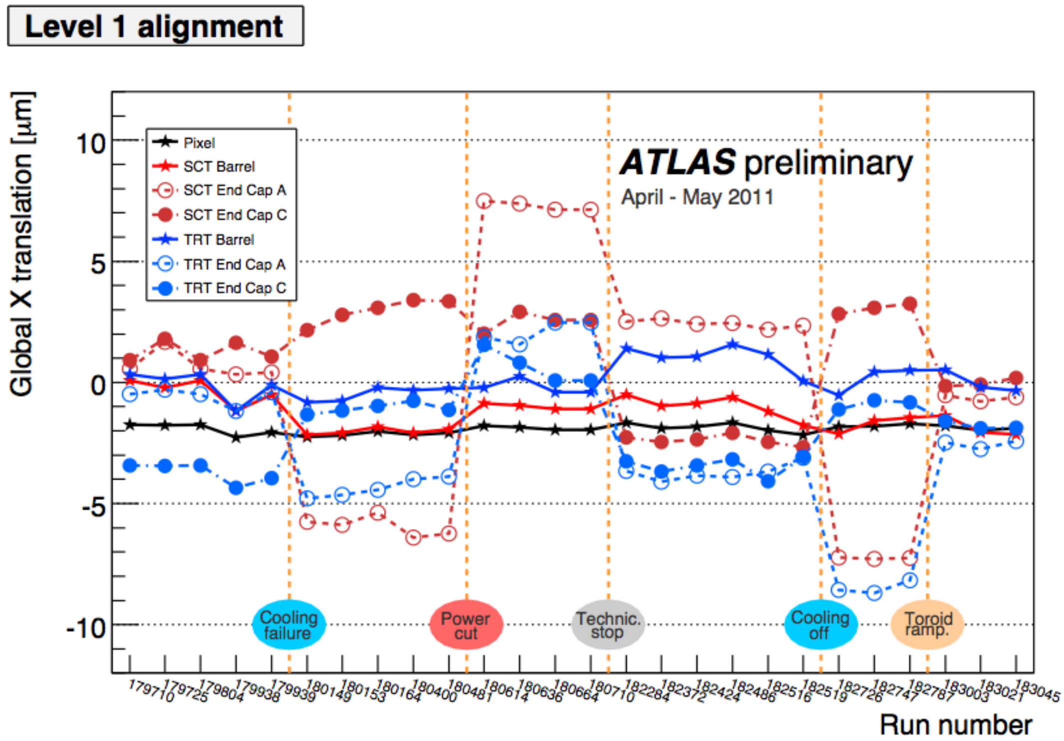

Figure 4.6: *Level One alignment corrections performed on a run by run basis starting from a common set alignment constants. The corrections shown are for translations in the global x direction.*

The most recent work in the ID Alignment group has been to try to remove, as much as possible, some of the systematic errors that our track based alignment algorithms have.

For example, some of the most important sources of systematic errors are the ones called weak modes. These weak modes are global distortions that preserve the helical trajectory of tracks and therefore leave the χ^2 unchanged. This is why our algorithms are totally blind to them and other methods are needed to deal with them. Some weak modes and their impact on physics measurements can be seen in Figure 4.7.

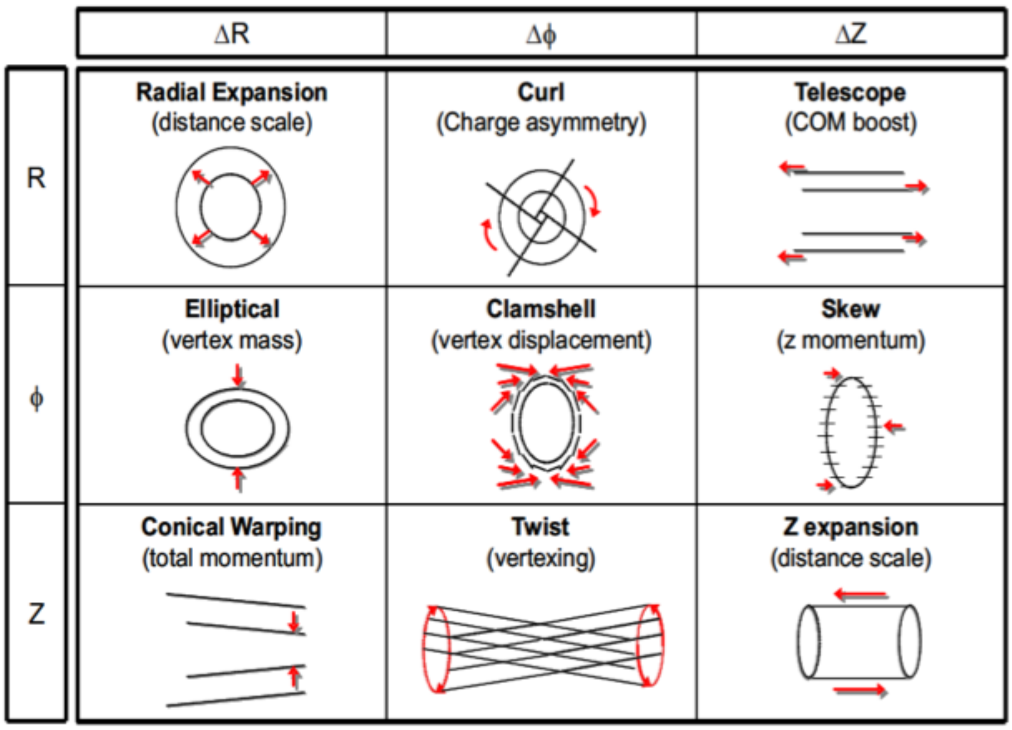

Figure 4.7: *Summary of possible systematic deformations*

Some of the methods that can be used for dealing with weak modes are, for example, using different samples of tracks (as it has been explained before collision and cosmic tracks have been used since the beginning of the ID Alignment to help with some of these systematic errors), using constraints such as invariant masses of well known resonant decays or the E/p of electrons[6]. In Figure 4.8 we can see the invariant mass distribution of Z → μμ decays. The shadowed area is the MC prediction for a perfectly aligned detector. The black dots are calculated with the Spring 2011 alignment constants and the red dots are calculated with the Summer 2011 alignment constants, when for the first time constraints derived from the E/p of electrons were included. The improvement using this constraint is clearly visible.

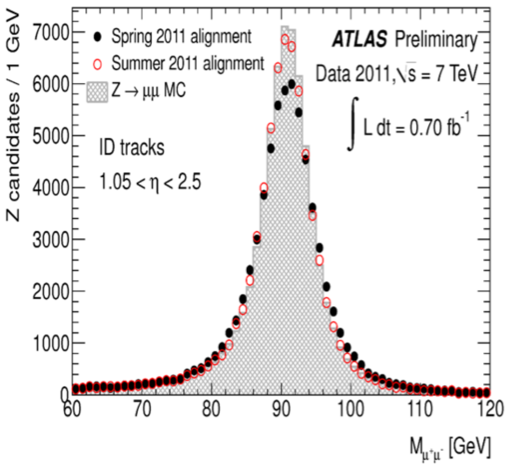

Figure 4.8: *Invariant mass distribution of Z → μμ decays, where the mass is reconstructed using track parameter from the Inner Detector track of the combined muons only.*

Another example of how invariant masses of well known resonant decays can help removing systematic errors can be seen in Figure 4.9

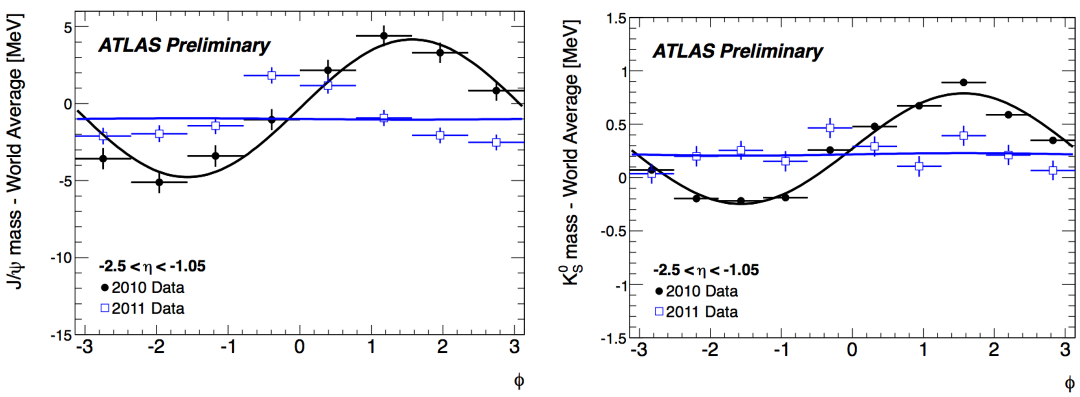

Figure 4.9: *The plot on the left shows the mean reconstructed mass for J/ψ candidates minus the world average J/ψ mass as a function of φ in the end-cap C of the ATLAS Inner Detector. The plot on the right shows the same for the K_s^0. The black dots are from 2010 data and the blue ones are from 2011 data. Both data points sets are fitted with a sinusoid.*

[6] The E/p of electrons and positrons is expected to be the same. A difference in the distributions would mean a bad measurement of the momentum, and therefore a deformation of the detector. What has been done in the Summer 2011 reprocessing is to measure the difference of the E/p distributions' peaks for e^+ and e^-, and then create a map of corrections based in these differences. Then these corrections are applied to our track parameters and a new set of alignment constants is calculated.

The figure shows the reconstructed mass for K_s^0 candidates and J/ψ candidates minus the world average mass of these two resonances as a function of ϕ. A mass bias as function of ϕ can be observed in the 2010 data and has been explained by a relative rotation of the solenoid field with the ID. This has been corrected by rotating the magnetic field in the reconstruction software by 0.55 mrad around the x-axis and has been taken into account for 2011 data collection. As it can be seen, the improvement is evident.

4.3 Alignment procedure

The ID alignment procedure uses as input the collision and cosmic-ray tracks samples described in the previous section. The raw ID data of the input events were used to reconstruct hit and cluster positions within the ID modules. Tracks were then found and fitted, allowing for computation of the track parameters and the track-hit residuals. The alignment algorithm was then run to obtain alignment constants that describe the correction to the detector geometry at each of the alignment levels. For this alignment, the initial knowledge of the ATLAS ID detector geometry was taken from the results of the previous alignment performed earlier in 2010 using cosmic-ray tracks and $\sqrt{s}$ = 900 GeV collision data.

As explained in section 4.2.4, the alignment is performed at different levels. The basic procedure for the alignment levels was the following:

- collision and cosmic-ray track samples were used in conjunction. A beam spot constraint was imposed for the collision tracks.
- All three ID subdetectors (pixels, SCT and TRT) were used in the track fitting.
- At each alignment level, several iterations were performed until convergence was reached.

The alignment at level 1 was performed using the degrees of freedom given in Table 4.1, aligning pixels, SCT and TRT simultaneously. The Global χ^2 alignment algorithm was used for this level. The size of the corrections was of the order of micrometres. This implies that the change in position of the ID subsystems during the 2009-2010 winter shutdown and the spring 2010 data taking was of that order of magnitude. This is an important indication of the level of detector stability.

The alignment was then performed at level 2 using the Global χ^2 algorithm. During initial iterations, the TRT structures were kept fixed whilst the silicon substructures were aligned. The corrections in the barrel layers were small, as in the level 1 case. However, the corrections of some SCT disks were up to 100 μm. The extent of these corrections was expected as this was the first time that the end-cap discs and wheels were aligned with large track statistics and high momentum tracks (hence reduced multiple Coulomb scattering effects).

In the second stage of the level 2 alignment, all three subdetectors were aligned simultaneously using the degrees of freedom given in Table 4.1. Some readjustment of the SCT and TRT end-cap wheels was observed as corrections of several tens of micrometres were obtained. Convergence was found after just three iterations. In order to verify that no structure movements were introduced by the alignment of the layers and discs, this alignment stage was complemented with an extra level 1 iteration. In this last iteration, the magnitude of the alignment corrections was sub-micrometre.

In the final step the alignment was performed at level 3. In this step the silicon modules and TRT wires were aligned separately. Due to the very large number of degrees of freedom involved, the Local χ^2 algorithm was used. Section 4.3.1 describes the silicon modules alignment, and Section 4.3.2 describes the wire-by-wire alignment in the TRT.

4.3.1 Alignment of the Silicon System at Module Level

The alignment of the individual silicon modules was performed in two stages. In both stages the TRT was fixed and only the silicon modules were aligned. The alignment technique applied was the Local χ^2 method, described in section 4.2.3. The main characteristics of the first stage of the silicon module alignment are the following:

- All the silicon modules (pixel and SCT, barrel and end-cap) were aligned.
- Only the most sensitive degrees of freedom (namely T_x, T_y and R_z) were considered.
- In order to increase the correlation between modules, the track selection was tightened. Only tracks intersecting two adjacent overlapping modules in at least one silicon layer (either the pixel or the SCT) were retained.
- Pixel modules were modelled as a perfect flat surface.

Several iterations of the Local χ^2 alignment were carried out at this stage. The overall corrections for the translation along the precise coordinate (T_x) were at a maximum 30 μm. Once this stage was completed, the TRT wire-by wire alignment was executed as described in Section 4.3.2.

After the completion of the TRT wire-by-wire alignment the second stage of the silicon module alignment was carried out. The main features of this stage were:

- Only the pixel barrel modules were aligned. The rest of silicon modules were fixed along with the TRT.
- All the degrees of freedom (except T_z) were used.
- Pixel modules were no longer modelled as a perfectly flat surface. Instead a distorted module geometry was used, according to the survey measurements of twist and/or bend of the detector wafers. It corresponds to out of plane corrections of the order of few tens of micrometres.

By including the measured pixel module distortions into the reconstruction the 3D coordinated of the measured hit position are corrected. The impact of the module distortions on the pixel residuals was sizable and was visible before any realignment was applied. Alignment of the pixel modules while enabling the pixel module distortions resulted in further improvements of the alignment results of the pixel modules. Further iterations were performed at this stage and resulted in corrections of a maximum 10 μm along the precise pixel coordinate. The effect of the alignment and the use of the distortions can be seen in Figures 4.10 (a) and (b). For the sake of clarity, the figure only shows a subset of the intermediate pixel barrel layer. It is possible to observe that some modules had internal variations of the average residual of up to 15 μm (fig. 4.10 (a)). These internal variations are reduced after the module distortions correction and the subsequent module level alignment (fig. 4.10 (b)).

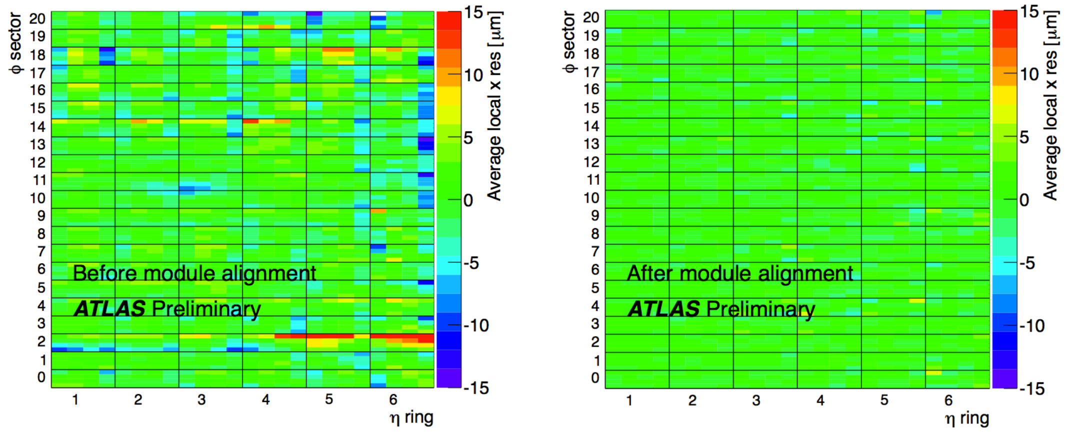

(a) *(b)*

Figure 4.10: *Detailed residual maps of the barrel pixel modules. Each pixel module has been split into a 4×4 grid and the average residual in each cell is plotted. Each module is identified by its position in the layer. This is given by its "η ring" and "φ sector" indices. The (a) figure shows the average local x residual before the module level alignment. Figure (b) shows the average local x residual after module level alignment (including pixel module distortions). Only a subset of the pixel modules of the intermediate pixel barrel layer is shown.*

4.3.2 TRT Wire-By-Wire Alignment Method

After the alignment of the TRT modules at level 2 an overall improvement in the track-hit residuals for the TRT modules was observed. Nevertheless, detailed maps of the mean of the residual distributions of the barrel and end-cap modules revealed internal structures that could not be removed by a level 2 alignment. Therefore a wire-by-wire alignment was performed in both barrel and end-cap TRT detectors.

Figure 4.11 (a) displays the mean of the TRT track-hit residuals as a function of φ-sector and z (along the wires) for the innermost TRT barrel layer. One can observe biases in the residuals of up to 80 μm that vary along the wires. This residual structure in z can only be removed by aligning the wires.

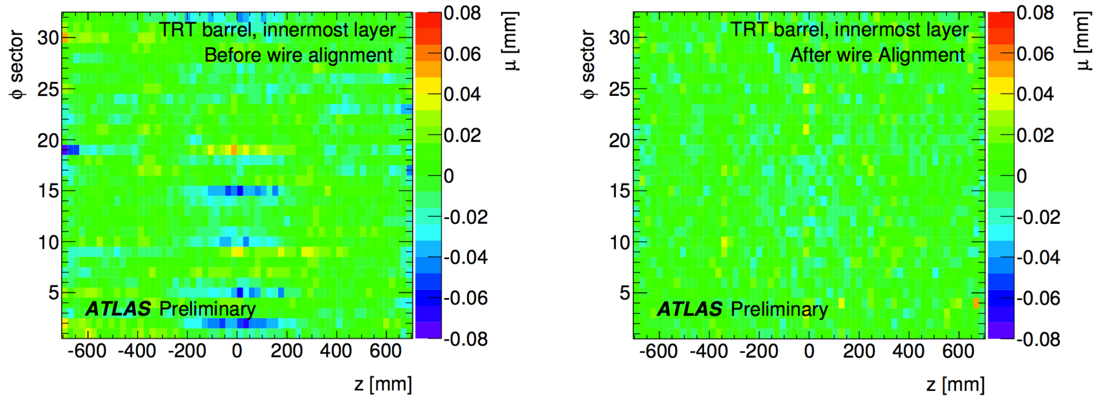

(a) *(b)*

Figure 4.11: *Mean of a Gaussian fit to TRT residuals vs. φ-sector and z for the first TRT barrel layer before, 4.11 (a), and after, 4.11 (b), the wire-by-wire alignment.*

A similar internal structure of the track-hit residuals was also observed in the end-cap wires. Figure 4.12 (a) shows the fitted mean of the TRT residual as a function of φ and end-cap wheel identifier. Within and en-cap wheel, there are regions with internal variations of the residual means of up to 150 μm. These regions vary continuously within the end-cap wheels and discontinuously across wheel boundaries. The residual variation in ϕ is oscillatory with two full periods over 2π. This pattern in the residual structure was thought to be the result of elliptical deformations of the end-cap wheels. Such deformations would be expected to be uncorrelated wheel-to-wheel given their independent construction, and cannot be described by either a translation or rotation of the whole wheel (level 2 alignment) as the internal wire alignment in each wheel is preserved at this level.

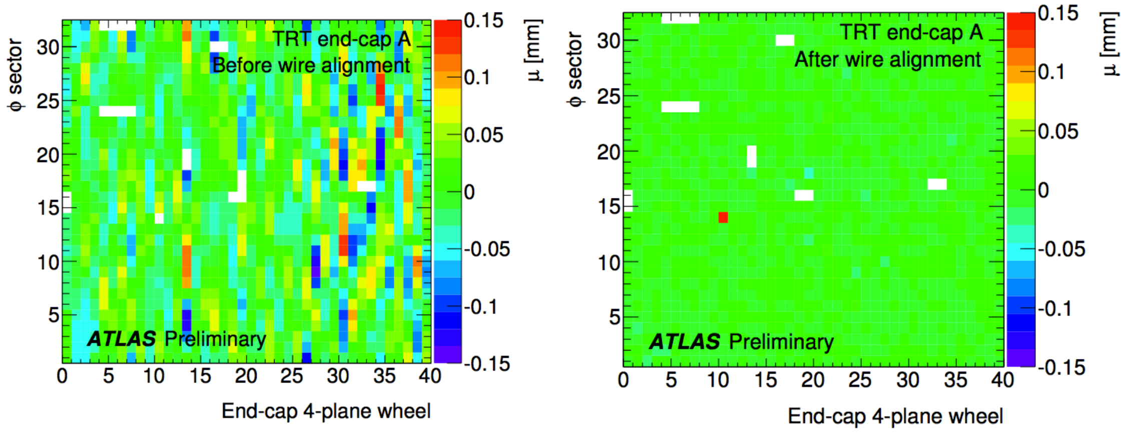

(a) *(b)*

Figure 4.12: *Mean of a Gaussian fit to TRT residuals vs. ϕ-sector and wheel before, 4.12 (a), and after, 4.12 (b), the wire-by-wire alignment. The plots illustrate the end-cap A results. The white bins are due to dead channels.*

The internal structure of the TRT end-cap module residuals can also be observed in a different view. Figure 4.13 (a) shows the fitted mean of the TRT residual as a function of radius and end-cap wheel. Within and end-cap wheel, the residual mean varies (up to 150 μm) continuously along the radius (r), and tends to oscillate in neighbouring wheels. This pattern in the residual structure is consistent with a ϕ rotation of the inner radius of the wheel with respect to the outer radius. The wheel-to-wheel oscillations can be explained by the way in which the wheels were assembled. Neighbouring wheels were constructed independently on the same assembly table, and pairs of end-cap wheels were then combined back-to-back and stacked to form the end-caps. A deformation in the machining table, giving rise to a twisting of the end-cap rings, would give rise to the observed wheel-to-wheel oscillatory pattern.

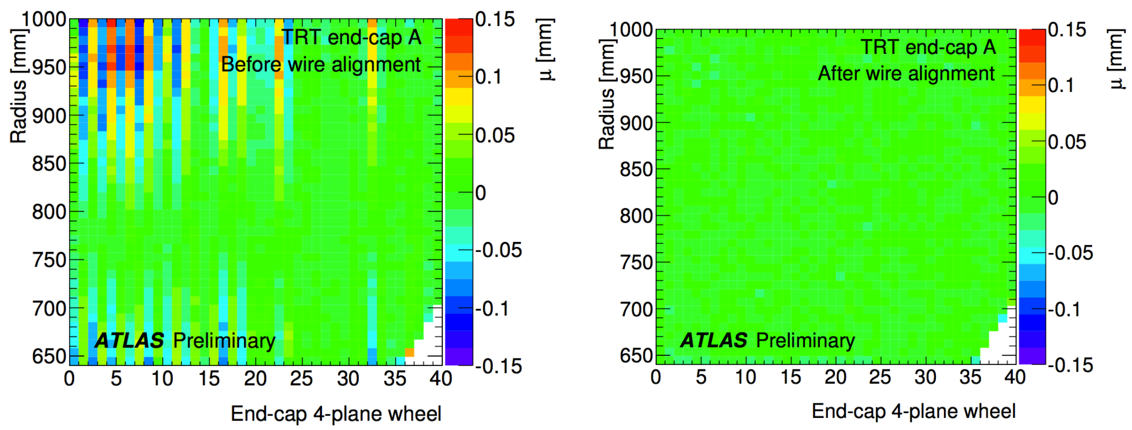

(a) *(b)*

Figure 4.13: *Mean of a Gaussian fit to TRT residuals vs. radius and wheel before, 4.13 (a), and after, 4.13 (b), the wire-by-wire alignment. The plots illustrate the end-cap A results. The white area in the lower right corner is due to acceptance effects.*

A wire-by-wire alignment was performed in order to correct the systematic variations shown in Figures 4.11 (a), 4.12 (a) and 4.13 (a). All of the TRT barrel and end-cap wires were aligned using just two degrees of freedom per wire (Table 4.1). In the barrel, the translations along $\hat{\phi}$ (T_ϕ) and rotations about $\hat{r}$ (R_r) were aligned. $\hat{\phi}$ represents the unit vector in the plane transverse to the beam direction at the wire position, whilst $\hat{r}$ denotes the radial direction in the transverse plane at the wire position. The end-cap degrees of freedom used were the translations along $\hat{\phi}$ (T_ϕ) and rotations about z (R_z). These degrees of freedom are those that correspond to movements of the wire in the sensitive direction, perpendicular to the track trajectory of tracks coming from the interaction point. The resulting alignment corrections correspond to wire movements of up to hundreds of micrometres.

This wire-by-wire alignment was performed using the collision tracks for several iterations until convergence in the alignment corrections was reached. The net improvement in the TRT residual distributions can be seen in Figures 4.11 (b), 4.12 (b) and 4.13 (b) which show the residual distributions after the wire-by-wire alignment. In all cases the residual structures are removed; the residuals after the wire-by-wire alignment are uniform across barrel and end-caps and do no show significant biases.

4.4 Alignment performance results

In this section some of the results which demonstrate the quality and performance of the ID alignment described in section 4.3 will be presented. This is referred to as the Autumn 2010 Alignment. For this purpose it was used a data-set that comprises ~150,000 events collected using a jet trigger from $\sqrt{s}$ = 7 TeV proton-proton collision runs taken between 29th July 2010 and 18th August 2010. This trigger requires a jet candidate object with $E_T > 55$ GeV at the first trigger level, and provides a good yield of relatively high p_T tracks which are more sensitive to the impact of the ID alignment. It is also interesting to note that this data set is independent of the one used to derive the Autumn 2010 Alignment (section 4.2.5). Unless otherwise stated, the data set is reconstructed using the Autumn 2010 Alignment. Each event used is required to have a primary vertex reconstructed with at least 3 tracks. The tracks used in this study are required to pass the following selection criteria:

- Number of Pixel hits ≥ 1.
- Number of (Pixel + SCT) hits ≥ 6.
- The following requirements are made of the transverse and longitudinal impact parameters with respect to the primary vertex position: $|d_0| < 1.5$ mm, $|z_0| < 1.5$ mm.

A transverse momentum requirement of either $p_T > 2$ GeV or $p_T > 15$ GeV is also made, dependent on the nature of the comparison. After these selection criteria the jet trigger data sample comprises ~ 2.3 million (~ 242,000) tracks with $p_T > 2$ GeV ($p_T > 15$ GeV). Note that unbiased hit-on-track residuals are used throughout this study.

4.4.1 Comparison to Initial ID Alignment

In this section the improvement in the ID alignment with respect to the initial ID alignment geometry is investigated. The jet trigger data sample is reconstructed using the Autumn 2010 Alignment, and this is compared to the same data sample reconstructed with the initial ID alignment, labelled Spring 2010 Alignment. The Spring 2010 Alignment was determined using a smaller sample of relatively low transverse momenta tracks from $\sqrt{s}$ = 900 GeV proton-proton collisions collected in December 2009.

Figure 4.14 compares the hit-on-track residual distributions obtained with the two different ID alignment setups for the Pixel, SCT and TRT barrel and end-cap modules. In the case of the Pixel and SCT, the residual shown is that in the local x direction (the projection of the residual onto the module local x direction). For these distributions the tracks are required to have p_T > 15 GeV. Shown is the full width half maximum (FWHM) of each distribution, divided by a factor 2.35 (for a Gaussian distribution the FWHM and standard deviation, σ, are related by σ = FWHM/2.35).

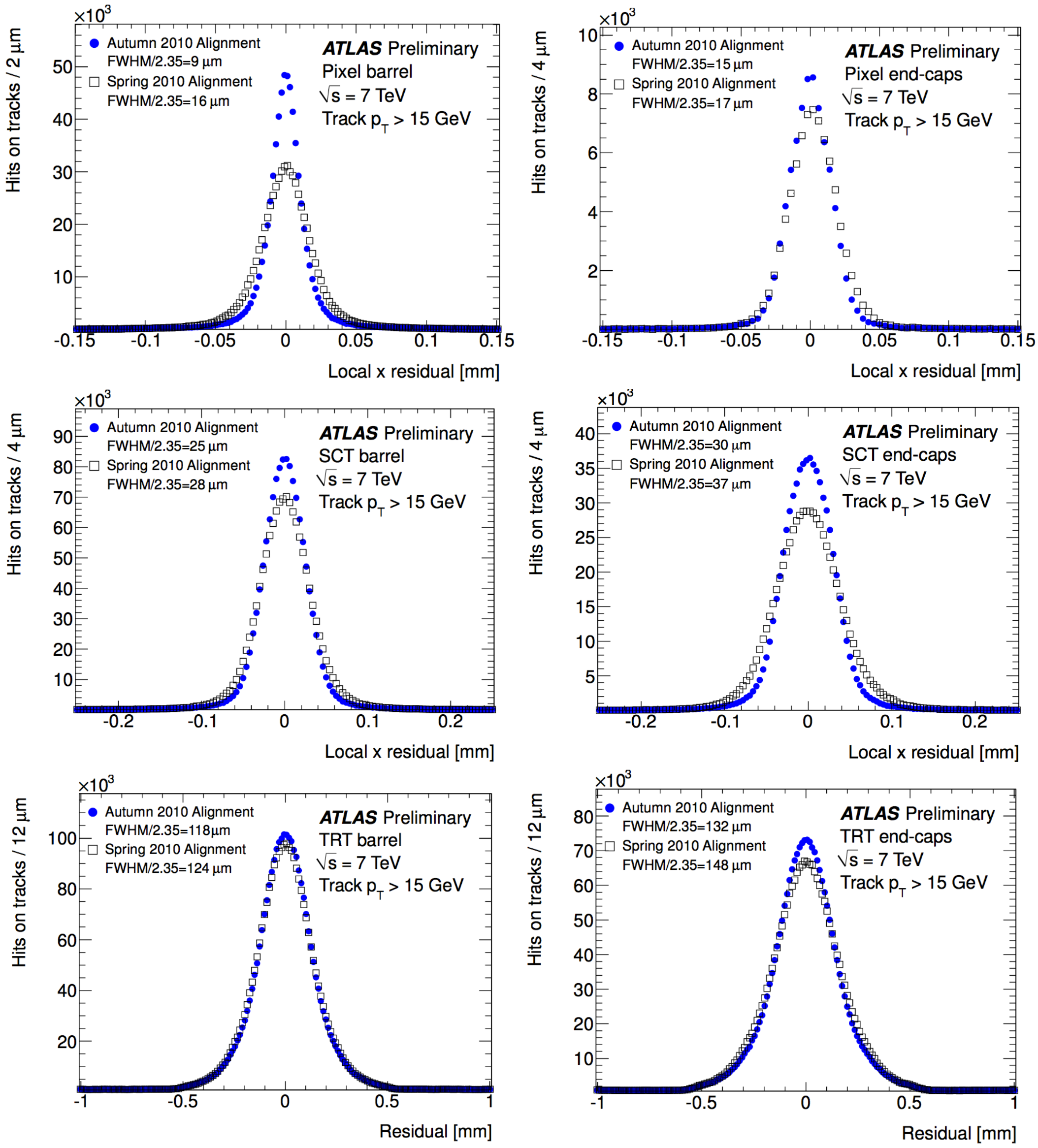

Figure 4.14: *Tracking local x unbiased residual distributions obtained by reconstructing the jet trigger data sample with the Spring 2010 Alignment (open squares) and Autumn 2010 Alignment (solid circles). The distributions are integrated over all hits-on-tracks in the Pixel barrel and end-cap modules (top), SCT barrel and end-cap modules (middle), and TRT barrel and end-cap modules (bottom). Tracks are required to have* p_T *> 15 GeV.*

In this comparison, for all the ID sub-detectors a narrower residual distribution is observed when using the Autumn 2010 Alignment. This relates directly to the overall improvement in the hit resolution for those modules. In order to more quantitatively asses the improvement in the alignment, one can perform a simple calculation to determine the additional resolution component (σ_{Diff}) that should have to be added in quadrature to the Autumn 2010 Alignment width (σ_{Autumn}) in order to reproduce the

Spring 2010 Alignment width (σ_{Spring}), $\sigma_{Diff} = \sqrt{\sigma^2_{Spring} - \sigma^2_{Autumn}}$. These results are reported in Table 4.2. As expected, the internal wire-by-wire alignment of the TRT barrel and end-caps (see Section 4.3.2), which introduced corrections to the wire positions of up to several hundred micrometres, has resulted in a substantial reduction of the contribution of misalignments to the effective TRT hit resolution. Large improvements in the alignment of the Pixel barrel, SCT barrel and SCT end-caps are also observed. In the case of the Pixel barrel modules, the use of the pixel module distortions in the reconstruction has a large impact. In the case of the SCT end-caps, a large component of the improvement derives from the significant corrections applied to the individual end-cap disks.

Detector	σ_{Spring} μm	σ_{Autumn} μm	σ_{Diff} μm
Pixel barrel	16	9	13
Pixel end-caps	17	15	8
SCT barrel	28	25	13
SCT end-caps	37	30	22
TRT barrel	124	118	38
TRT end-caps	148	132	67

Table 4.2: *Estimated resolution improvement with Autumn 2010 Alignment, σ_{Diff}, as described in the text. The Pixel and SCT results are for the precision (local x) coordinate.*

4.4.2 Comparison to Monte Carlo Simulation

In this section the jet trigger data sample reconstructed with the Autumn 2010 Alignment is compared to a dijet Monte Carlo (MC) event sample generated using PYTHIA and simulated using the GEANT4 ATLAS detector simulation. The simulation is done using a detector model in which the ID modules are in their nominal positions and orientations, and subsequently reconstructed using exactly the same geometry. Hence, the MC sample is reconstructed with "perfect" ID alignment. The same track reconstruction setup and track selection requirements are used on the MC and data samples. In addition, the dijet MC sample events are required to pass the same (simulated) jet trigger that was used to collect the jet trigger data sample. Where appropriate, the MC has been normalised to the number of entries in the data distributions.

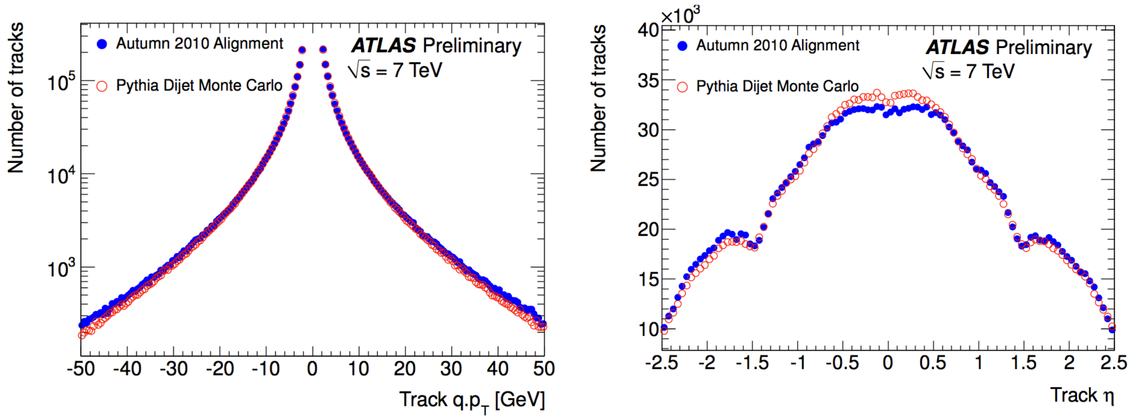

Figure 4.15: *Track p_T and η distributions of the jet trigger data and dijet MC simulation samples. The p_T distribution is signed with the charge (q) of the particle.*

Many of the observables are dependent on the p_T and η distributions of the input tracks. For example, due to the impact of multiple scattering the width of hit-on-track residual distributions is strongly dependent on the p_T spectra of the tracks, and also on the η distribution of the tracks, due to the differing intrinsic resolutions of ID modules traversed by the tracks at different rapidity regions. Therefore, in order to draw fair conclusions about the ID alignment performance, one should ensure that real data and MC p_T and η distributions are in reasonable agreement. Figure 4.15 shows the comparison of the track p_T and η distributions for the jet trigger data and MC samples. The agreement between the real data and MC distributions is good.

As it has been emphasized in this master thesis, the residual distributions are very important for the ID Alignment, so a comparison of the real residual distributions with the MC ones will give us very valuable information about the status of the ID alignment. For this reason the hit-on-track residual distributions for the jet trigger data and MC samples are compared in this section. For these distributions the tracks are required to have p_T > 15 GeV. This requirement is made to limit the impact of multiple scattering (and hence the material description) on the effective hit resolution, such that the observed width of the residual distribution is dominated by the ID alignment.

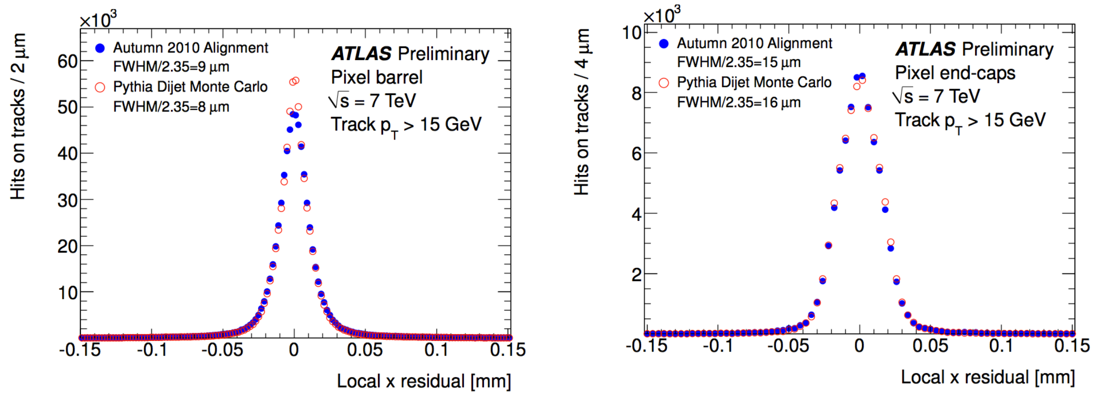

Fig 4.16: *The Pixel local x residual distributions for the jet trigger data sample reconstructed with the Autumn 2010 Alignment (full circles), compared with the dijet MC simulation sample (open circles). The distributions are integrated over all hits-on-tracks in barrel modules (left) and end-cap modules (right). Tracks are required to have p_T > 15 GeV.*

Figure 4.16 shows the local x residual distribution for all hits-on-tracks in Pixel barrel modules (left), and Pixel end-cap modules (right). Figure 4.17 shows the local y residual distributions (the projection of the residual onto the module local y direction) for Pixel barrel and end-cap modules, while Figure 4.18 shows the local x residual distribution for SCT barrel and end-cap modules. Figure 4.19 shows the residual distributions for TRT barrel and end-caps. Under the assumption that the MC simulation models perfectly the intrinsic hit resolution and the contribution of multiple Coulomb scattering (MCS), the difference in the observed residual width between the MC simulation and the data can be related directly to the contribution of residual misalignments in the data. In the case of the Pixel end-cap, SCT end-cap and TRT barrel modules, one can see that the data and MC simulation residual distributions agree very well. In the case of the Pixel barrel, SCT barrel and TRT end-cap modules, the slightly larger residual widths observed in the data imply relatively small residual misalignments that continue to degrade the hit resolution in these areas of the detector.

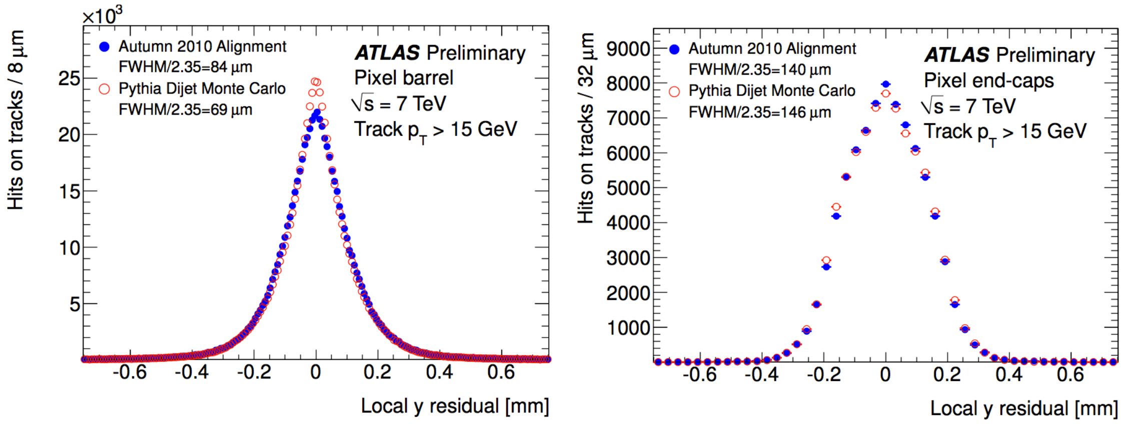

Figure 4.17: *The Pixel local y residual distributions for the jet trigger data sample reconstructed with the Autumn 2010 Alignment (full circles), compared with the dijet MC simulation sample (open circles). The distributions are integrated over all hits-on-tracks in barrel modules (left) and end-cap modules (right). Tracks are required to have $p_T > 15$ GeV.*

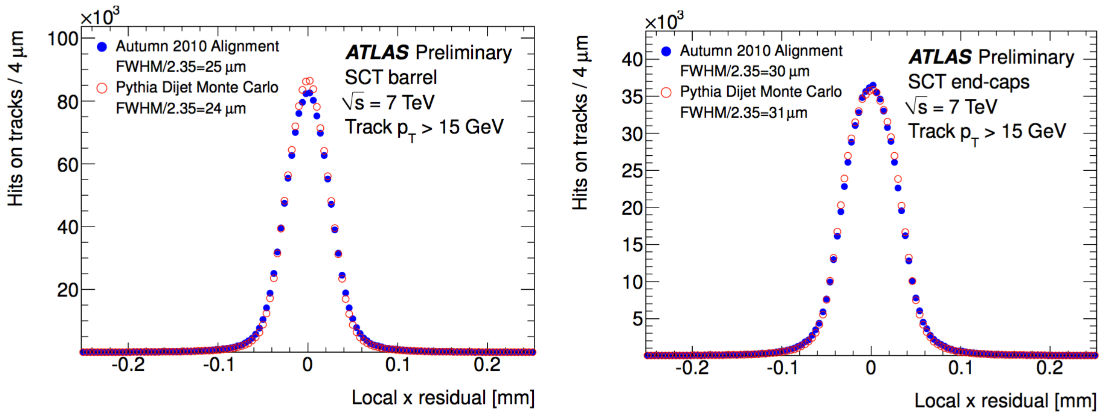

Figure 4.18: *The SCT local x residual distributions for the jet trigger data sample reconstructed with the Autumn 2010 Alignment (full circles), compared with the dijet MC simulation sample (open circles). The distributions are integrated over all hits-on-tracks in barrel modules (left) and end-cap modules (right). Tracks are required to have $p_T > 15$ GeV.*

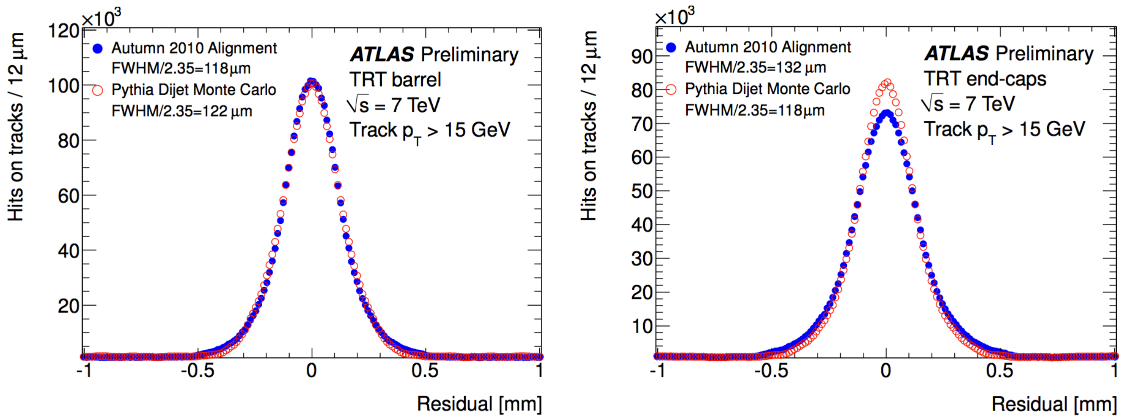

Figure 4.19: *The TRT residual distributions for the jet trigger data sample reconstructed with the Autumn 2010 Alignment (full circles), compared with the dijet MC simulation sample (open circles). The distributions are integrated over all hits-on-tracks in barrel modules (left) and end-cap modules (right). Both precision and non-precision (tube) hits are used. Tracks are required to have p_T > 15 GeV.*

In order to investigate further the impact of MCS effects on these conclusions, in Figure 4.20 the FWHM/2.35 of the residual distributions are plotted as a function of track p_T for p_T > 2 GeV. One can see that (due to the decreasing impact of the MCS) the residual width decreases as track p_T increases, until we reach an asymptotic limit, where the residual width is determined by the contributions of the intrinsic resolution and, in the data, module misalignments. Above p_T > 15 GeV, the MCS contribution is strongly suppressed and the data-simulation discrepancy is likely to be due to remaining module-to-module misalignments.

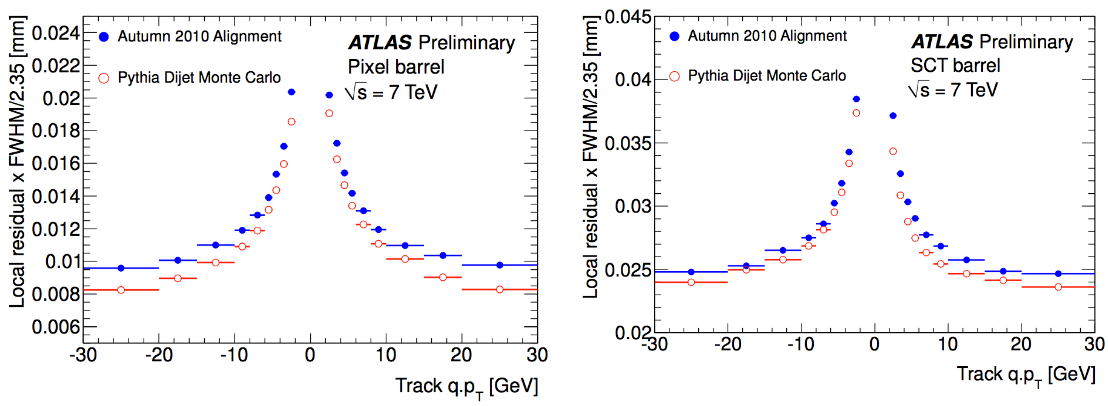

Figure 4.20: *The FWHM/2.35 width of the residual distributions for modules in the Pixel and SCT barrels as a function of track p_T. The residual distributions for the jet trigger data sample reconstructed with the Autumn 2010 Alignment (full circles) are compared with the dijet MC simulation sample (open circles).*

If a module layer in the barrel or a disk in the end-caps is misaligned with respect to the others the hits in that layer/disk will be systematically displaced from their true position, and the mean of the residual distribution for that layer or disk will be significantly different from zero. Figure 4.21 shows the mean of the residual distributions as a function of the module layer in the Pixel and SCT barrels, and as a function of the module disk in the Pixel and SCT end-caps. Since the mean of the residual distribution is not dependent on the track p_T, for these distributions the tracks are required to have p_T > 2 GeV. One can see that in the case of the Pixel and SCT barrel and end-cap layers, very small biases at the sub-micrometre level can be observed.

Remember that the runs used to analyse the alignment performance are independent from the runs used to derive the alignment constants. The origin of these small biases may be related to relative movements of the ID layers and disks at the level of 5 μm between different run periods.

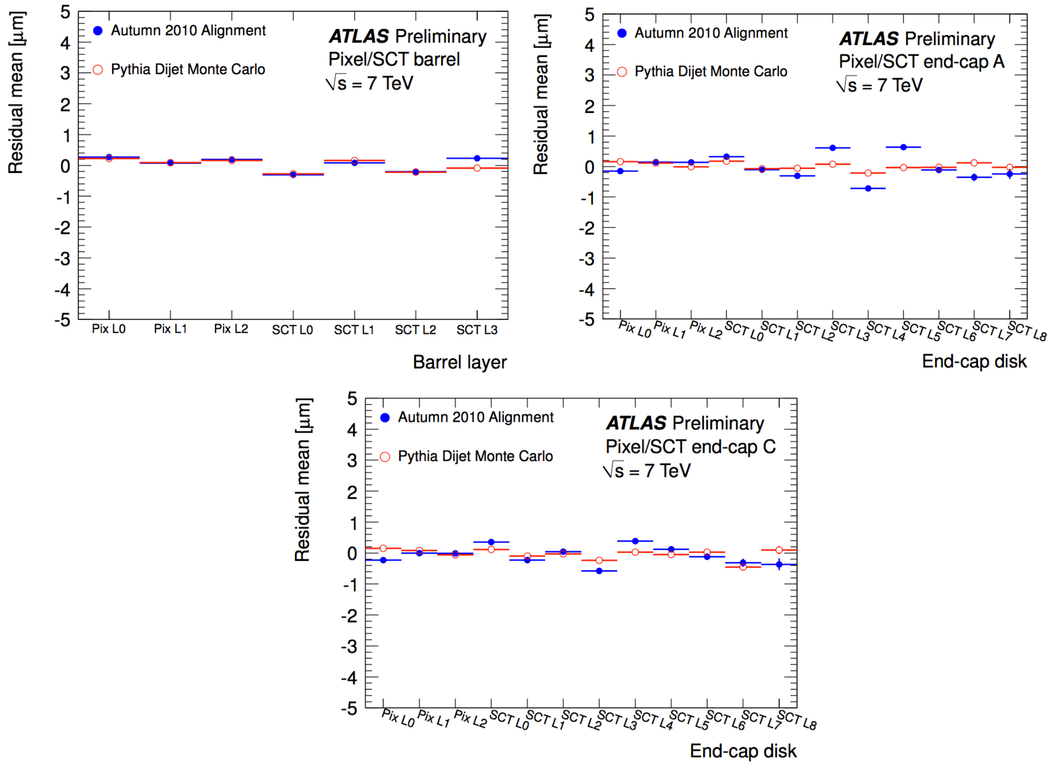

Figure 4.21: *Mean of the residual distributions as a function of the module layer in the Pixel and SCT barrels, and as a function of the module disk in the Pixel and SCT end-caps. The residual distributions for the jet trigger data sample reconstructed with the Autumn 2010 Alignment (full circles) are compared with the dijet MC simulation sample (open circles). Tracks are required to have* $p_T > 2$ *GeV.*

5 Inner Detector Alignment Monitoring

To understand the ID Alignment monitoring it would be useful to briefly explain the ATLAS Software: Athena. Athena is the name of the ATLAS software framework. Its code is based on the C++ language and it provides a facility for various needs such as event generation, reconstruction or detector description. Thus, it consists in a huge amount of algorithms organized in packages. Moreover, it ensures that the requested algorithms run in the correct order, and it offers common services like message logging, access to data on disc or remote disc servers and filling of histograms and ntuples. The handling of input/output data as well as the usage of services and algorithms is done in so-called *jobOption* files which are written in Python, another object-orientated, interpreted scripting language.

ATLAS software is organized into a hierarchical structure of packages. Each package contains services and algorithms where each package has a defined dependency on other packages. All these packages are managed and stored in a version control repository, in particular, SVN (Subversion) software. These kind of infrastructures are mandatory needed in order to work efficiently in a so high collaborative environment as ATLAS, where many scientists can be working in the same algorithm at the same time worldwide. Each package has a tag number which distinguishes between different versions. A project consists of a complete collection of tagged packages and it is identified with a release number.

Furthermore, the offline software contains a complete description of the ATLAS detector which is used by event data model for simulations and reconstructions. This part of the software has the information about the geometry and material of the detector, such as material properties and the position and orientation of detector elements. All the simulation and reconstruction steps in ATLAS get the detector information from a common source, called GeoModel, that ensures that each step uses exactly the same information (volumes and materials), thus preventing inconsistencies. The alignment software is integrated into this framework. At the same time, the event reconstruction is performed by a collection of algorithms and tools that perform raw data reconstruction, tracking and calibrations and so on.

Another important part from the alignment point of view are the databases. Several databases are needed in order to allow the Athena framework to succeed. Thus, for example, the numbers that define the size and position of each volume (needed by GeoModel) are stored in a database. Also, the alignment constants are stored in a conditions database which is used by the detector description to correct the nominal positions of the sensors from the previous database.

Now coming back to the ID Alignment Monitoring, among the packages mentioned before, there are two especially important for the ID Alignment, they are called InDetAlignmentMonitoring and InDetAlignGlobalChi2Monitoring. The first one is dedicated to validating the ID Alignment. It is the one that produces all the histograms that have been showed since section 4.3. And the second one contains a tool that plots automatically all the histograms that are needed for the ID Alignment. So, with these two packages the ID Alignment group is capable to monitor all the relevant parameters to align the ID.

Some of the most recent histogram in these two packages are worth it to comment:

- The average of the BeamSpot Position vs. Luminosity Block (LumiBlock)
- The average of the Tilt angles vs. LumiBolck
- The BeamSpot Position coordinates (Y vs. X, X vs. Z and Y vs. Z)
- The average of Biased and Unbiased X and Y Residuals vs. the Module Phi Identifier of the Pixel end-caps for each disk separately.

First of all it needs to be explained what the Beam Spot (BS) and tilt angles are.

The **beam spot** is the size of the luminous region. This is not the same as the size of the LHC beams and the LHC bunch length, since it is given by the overlap integral of the two beams. It is reconstructed as the average mean and width of the primary vertices distributions and monitored either online and offline.

The above so-called **tilt angles** are the angles of the BS with respect to the X and Y axis of the global coordinate system.

Although the BeamSpot group has a web page where one can find the BeamSpot Position and Tilt angles vs. LumiBlock, the ID Alignment Group considered it would be very useful to create its own plots given that these parameters are used as constraints for the alignment (i.e. these parameters are an important part of the input used for the alignment). This is a way of monitoring our input and testing if it is correct.

Figure 5.1 shows the average of the beam spot position coordinates in function of the luminosity block for run 180636. And Figure 5.2 shows on the top the Tilt X (which is the angle of the BS with respect to the X axis of the global coordinate system) in function of the luminosity block for the same run. And at the bottom, the same with the Tilt Y.

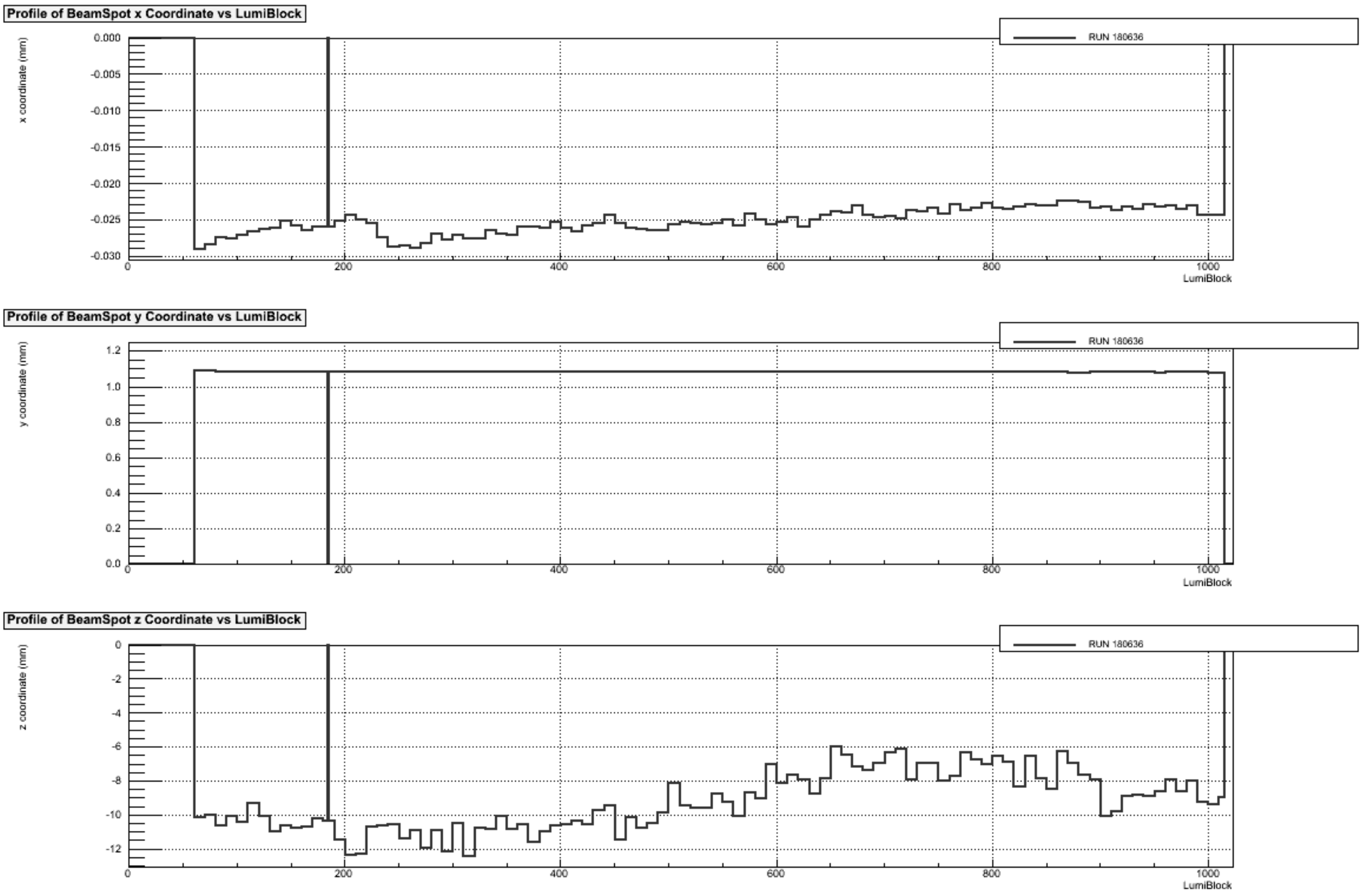

Figure 5.1: *Average of the beam spot position versus LumiBlock for run 180636. On the top we can see the x coordinate, in the middle the y and at the bottom the z.*

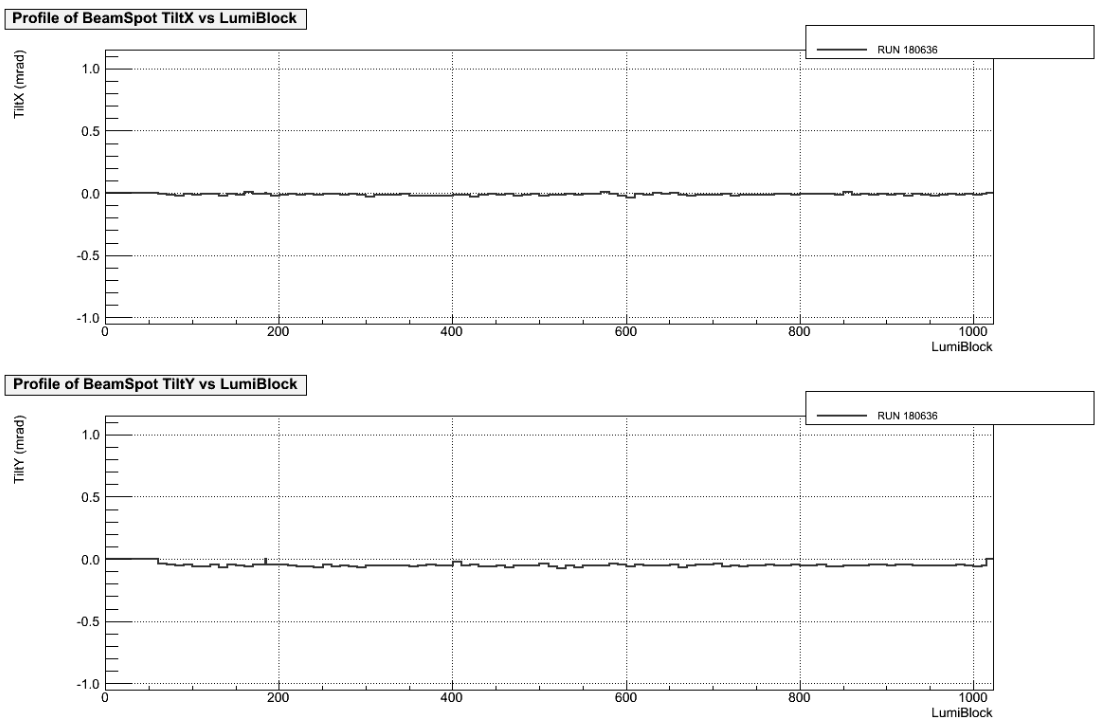

Figure 5.2: *Tilt angles vs. LumiBlock for run 180636. On the top we have the Tilt X and at the bottom the Tilt Y.*

Figures 5.3 and 5.4 show the plots representing the same quantities than Figure 5.1 and 5.2 but taken from the BeamSpot web application. We can see that both sets of histograms are in agreement, so this is a test that the new ID Alignment Monitoring plots are fine. (It has to be considered that the scales are different in the different sets of histograms. This is due to the reason that, from the Alignment point of view, it was better to haver a generic scale to have included the variations between different runs).

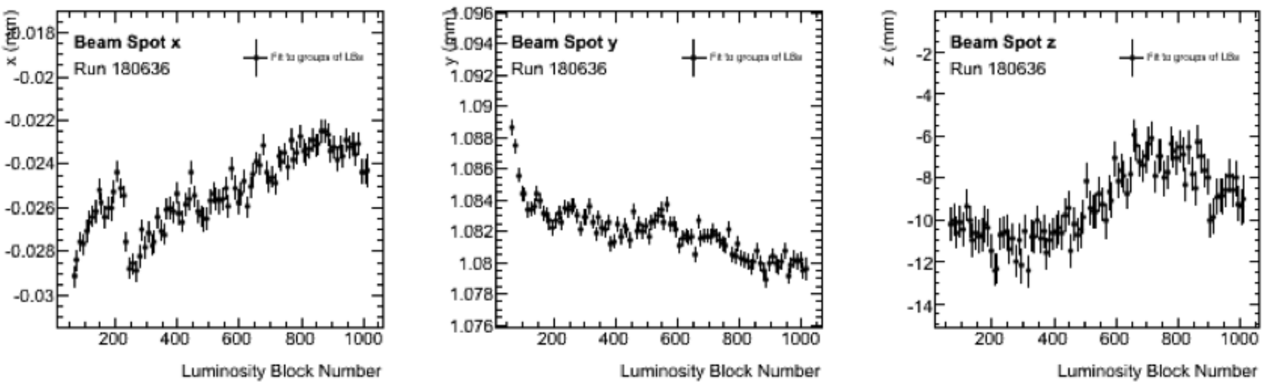

Figure 5.3: *Beam spot position coordinates in function of the Luminosity Block for run 180636 taken from the BeamSpot web page. The x coordinate is in the left part, the y coordinate in the middle and the z coordinate in the right part of the figure.*

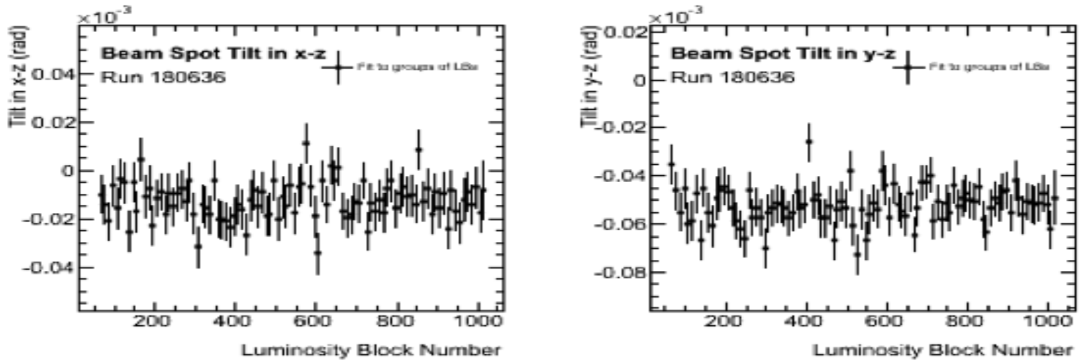

Figure 5.4: *Tilt angles vs. LumiBlock for run 180636 taken from the BeamSpot web page. On the left side we have the Tilt X and on the right side the Tilt Y.*

Another thing that is very useful to represent is the beam spot position coordinates against one another, this way it is very easy to see the shape of the beam spot in a run if the two coordinates are drawn with the same scale.

Figure 5.5 shows the X coordinate of the BS in function of the Z coordinate of the BS, Figure 5.6 shows Y vs Z and Figure 5.7 shows Y vs X. All of them have been plotted for the entire run 180636.

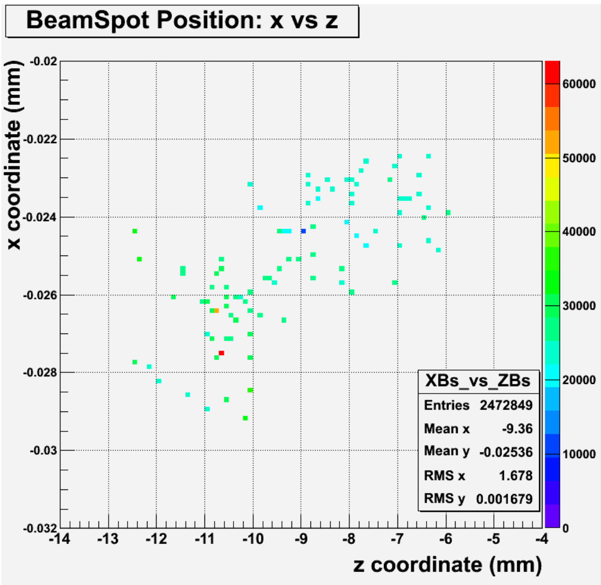

Figure 5.5: *Beam spot coordinate x in function of coordinate z for run 180636.*

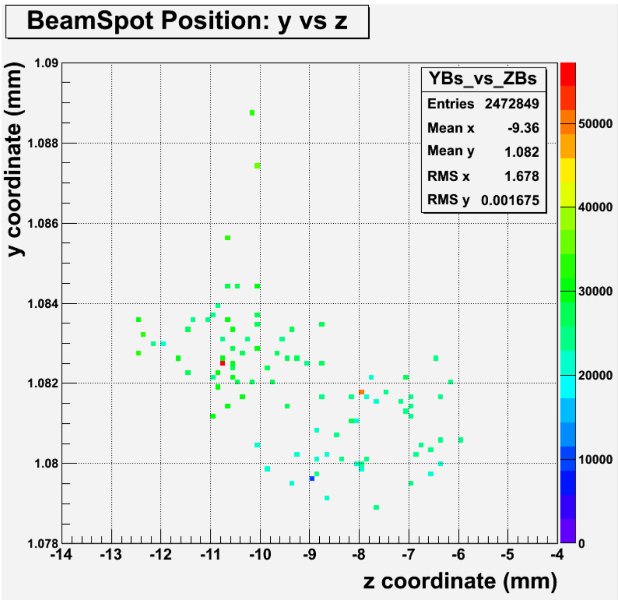

Figure 5.6: *Beam spot coordinate y in function of coordinate z for run 180636.*

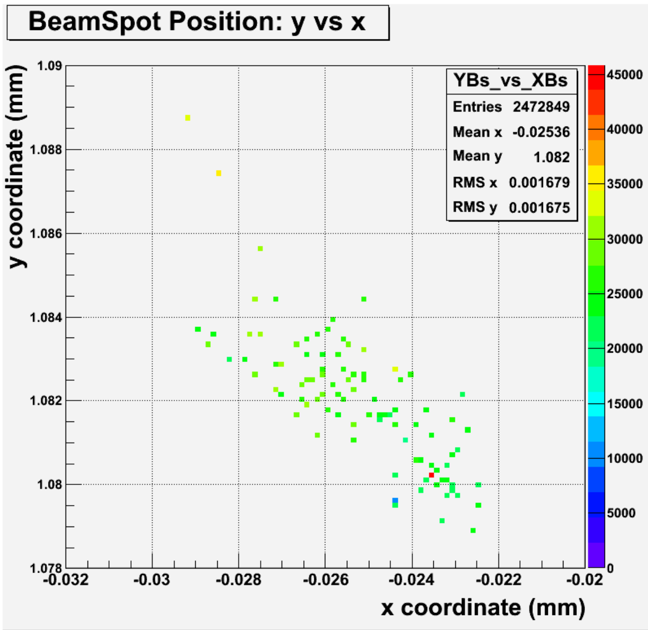

Figure 5.7: *Beam spot coordinate y in function of coordinate z for run 180636.*

The other new plots in the packages are the average of biased and unbiased X and Y residuals in function of the Module Phi Identifier[7] of the Pixel end-caps for each disc separately. Previous to these improvements in the package one could only access these plots with the three discs together. Having a different histogram for each disc will be very useful to study them with more detail and to monitor the movements of the different discs more consistently.

Figure 5.8 shows the histogram of the X residual in function of a modified Module Phi Identifier with the three disks of the pixel end-cap A in the same plot. This picture has been taken from the Data Quality Monitoring (DQM) web page.

[7] The Module Phi Identifier is a number that is assigned to each module of the Pixel end-cap discs in function of its ϕ position.

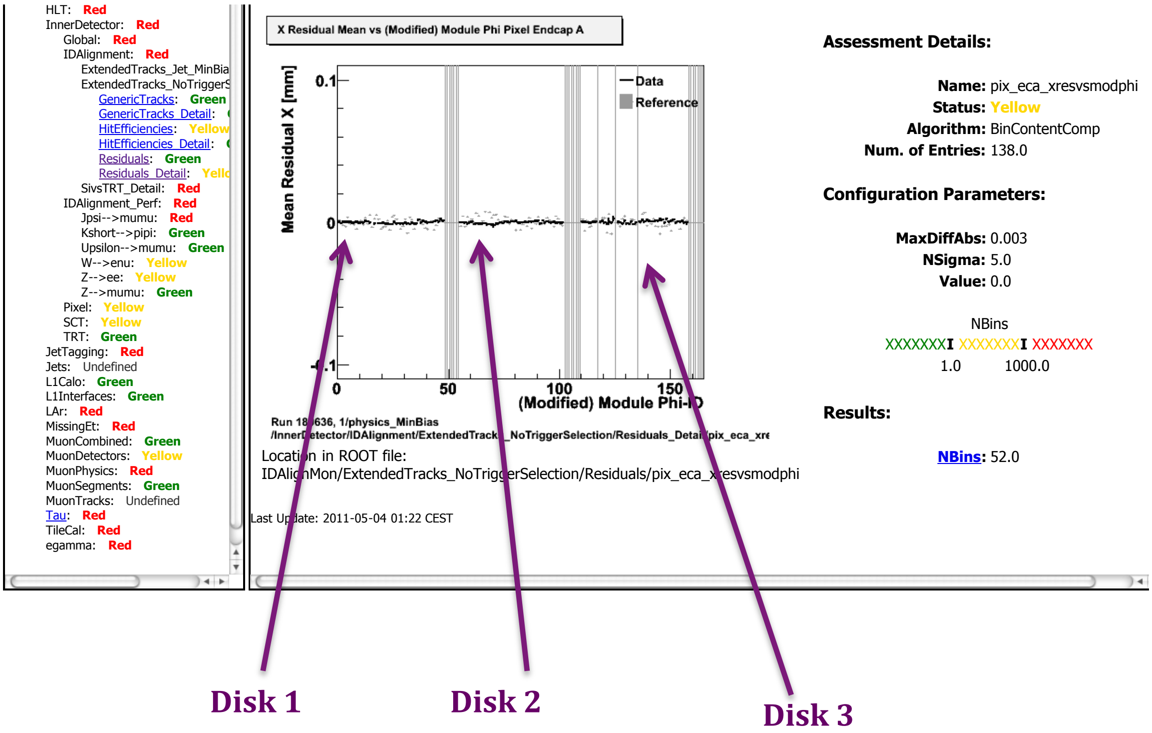

Figure 5.8: *Average X unbiased residual vs. (Modified) Module Phi Identifier of the Pixel End-cap A. Screen shot taken from the DQM web page.*

The improvement in the kind of plot that we see in Figure 5.8 is, as it has been said before, that now there is one histogram for each disk of the Pixel end-caps. Figures from 5.9 until 5.16 show the biased and unbiased x and y residuals in function of the Module Phi Identifier for each disk separately for Pixel end-caps A and C. These residual plots have been calculated with all the data of the runs 180614, 180636, 180664 and 180710. And they have been calculated with two different sets of constants, the red lines (or dots) correspond to the constants tagged as InDetAlign_Collision_7T_2011_03, which was the first set of alignment constants calculated with 2011 data. They were calculated with the data collected until March 2011. The second set is marked with the black lines (or dots) and correspond to the ones tagged as InDetAlign_Collision_7T_2011_05, which were calculated with data collected until May 2011.

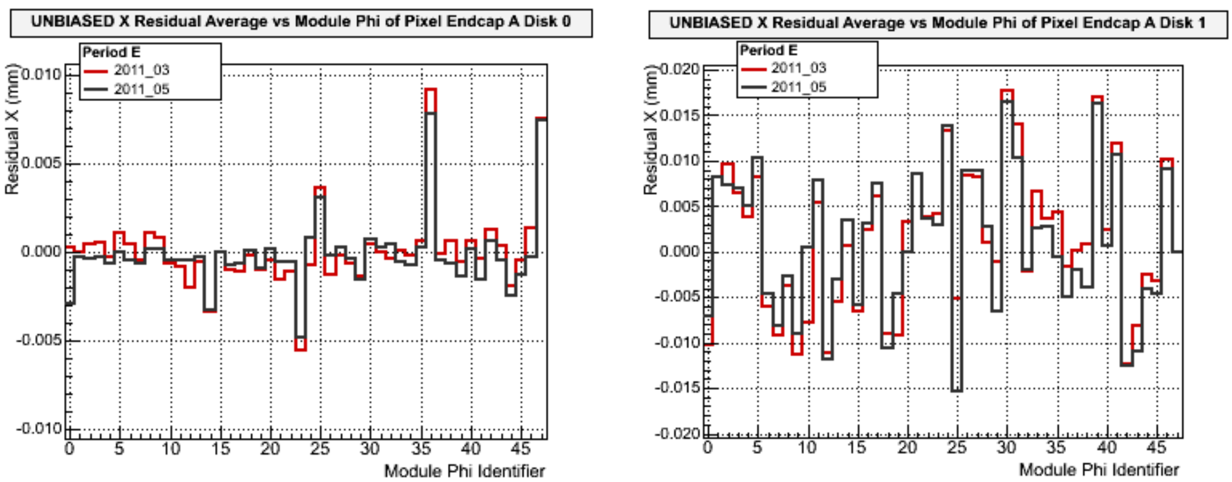

(a) (b)

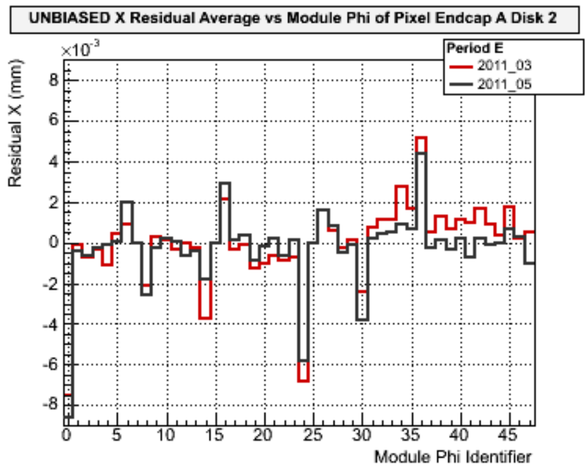

(c)

Figure 5.9: *Averaged **unbiased x** residuals vs. Module Phi Identifier of Pixel **end-cap A** where (a) is disk 0, (b) is disk 1 and (c) is disk 2.*

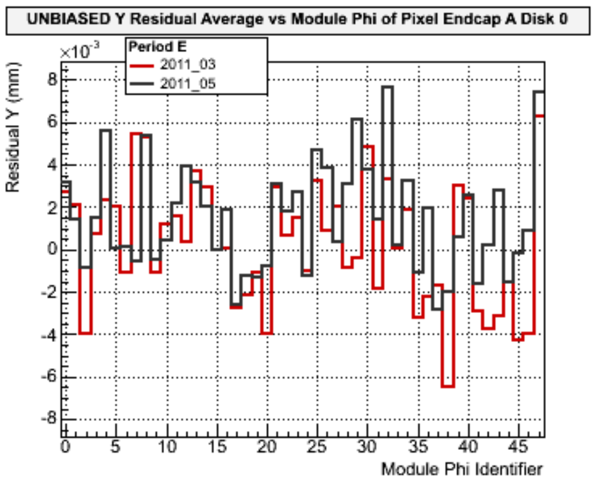

(a)

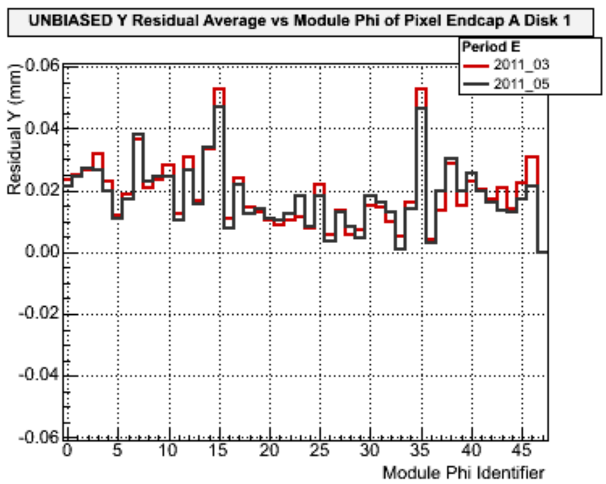

(b)

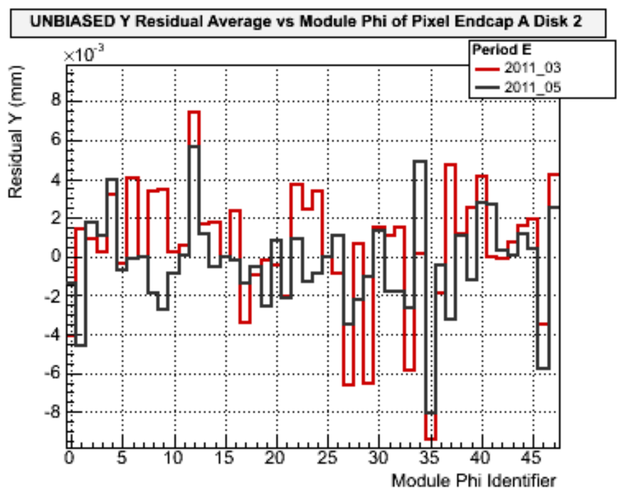

(c)

Figure 5.10: *Averaged **unbiased y** residuals vs. Module Phi Identifier of Pixel **end-cap A** where (a) is disk 0, (b) is disk 1 and (c) is disk 2.*

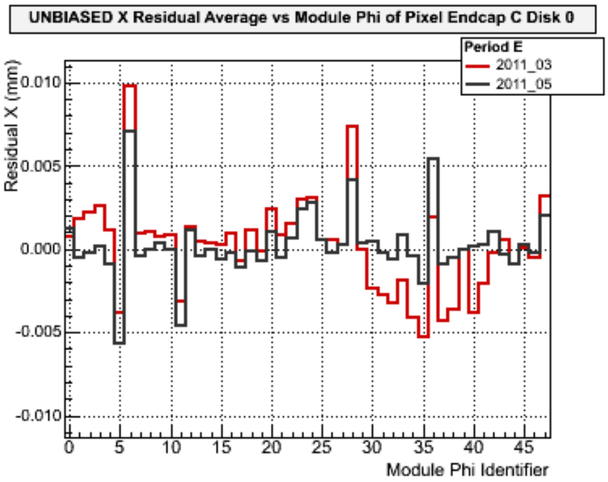

(a)

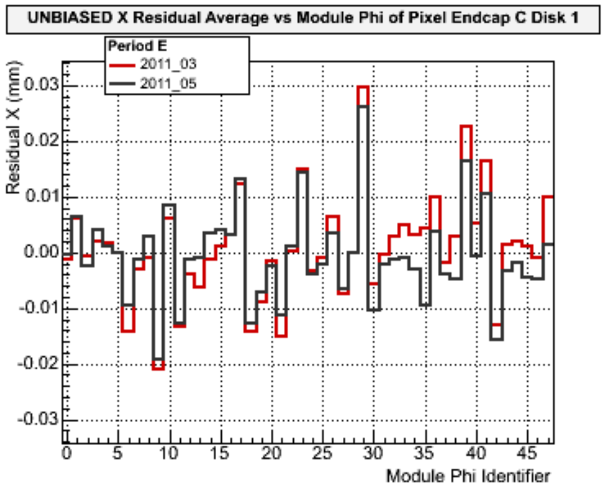

(b)

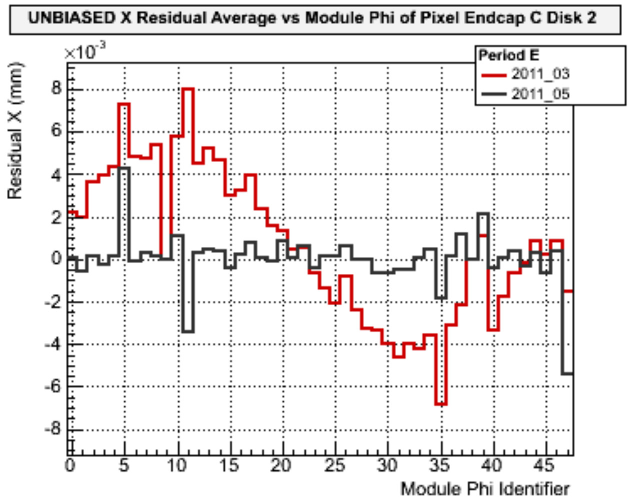

(c)

Figure 5.11: *Averaged* ***unbiased x*** *residuals vs. Module Phi Identifier of Pixel* ***end-cap C*** *where (a) is disk 0, (b) is disk 1 and (c) is disk 2.*

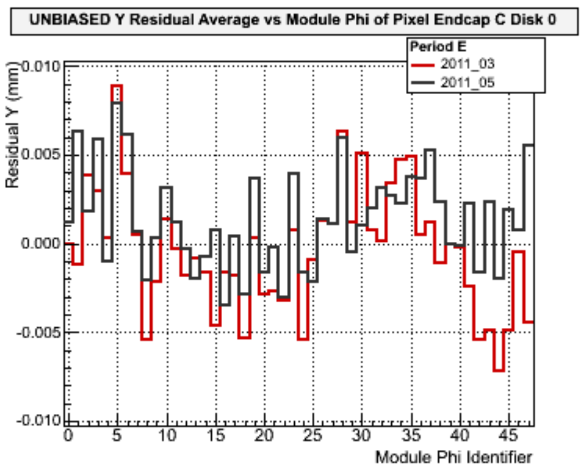

(a)

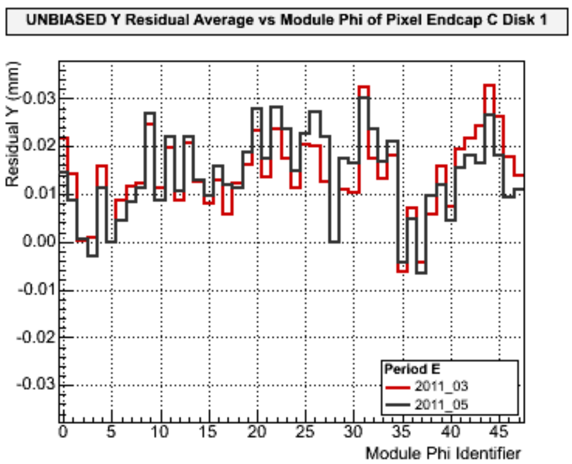

(b)

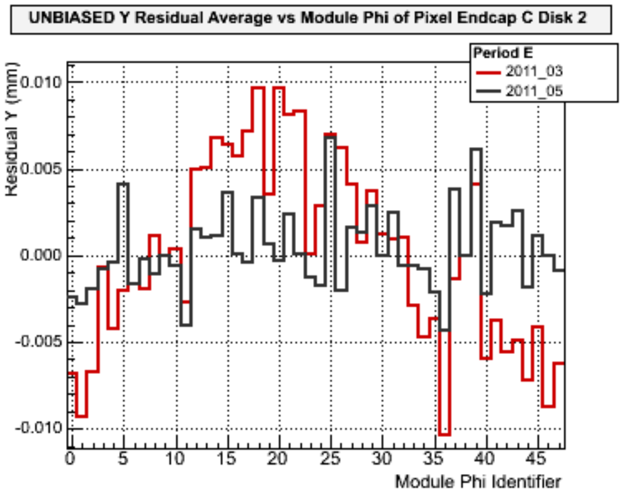

(c)

Figure 5.12: *Averaged* ***unbiased y*** *residuals vs. Module Phi Identifier of Pixel* ***end-cap C*** *where (a) is disk 0, (b) is disk 1 and (c) is disk 2.*

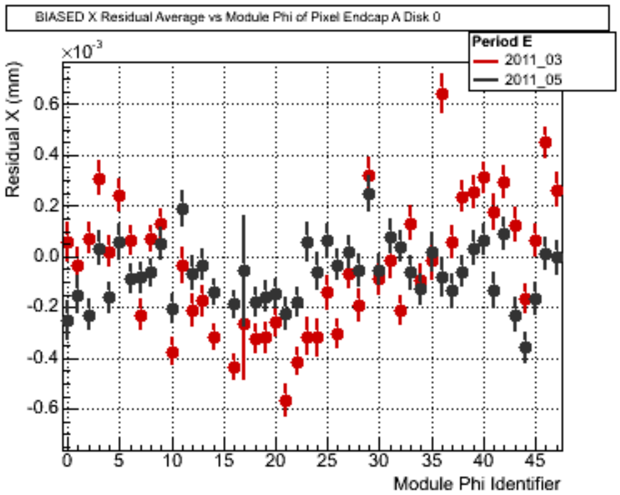

(a)

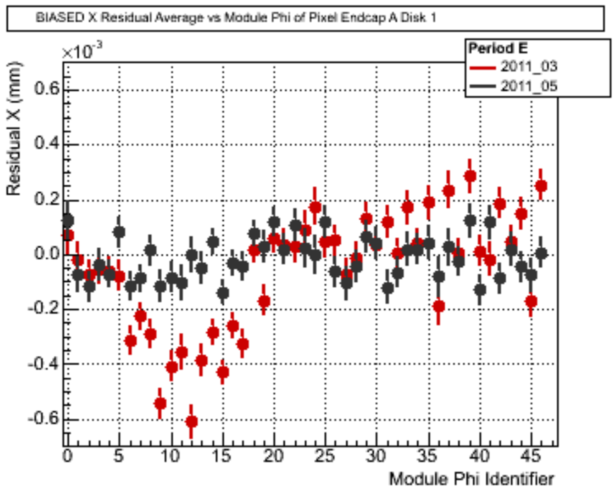

(b)

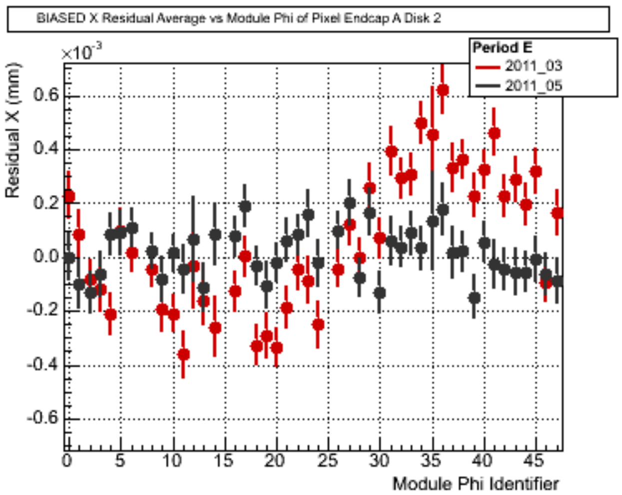

(c)

Figure 5.13: *Averaged* ***biased x*** *residuals vs. Module Phi Identifier of Pixel* ***end-cap A*** *where (a) is disk 0, (b) is disk 1 and (c) is disk 2.*

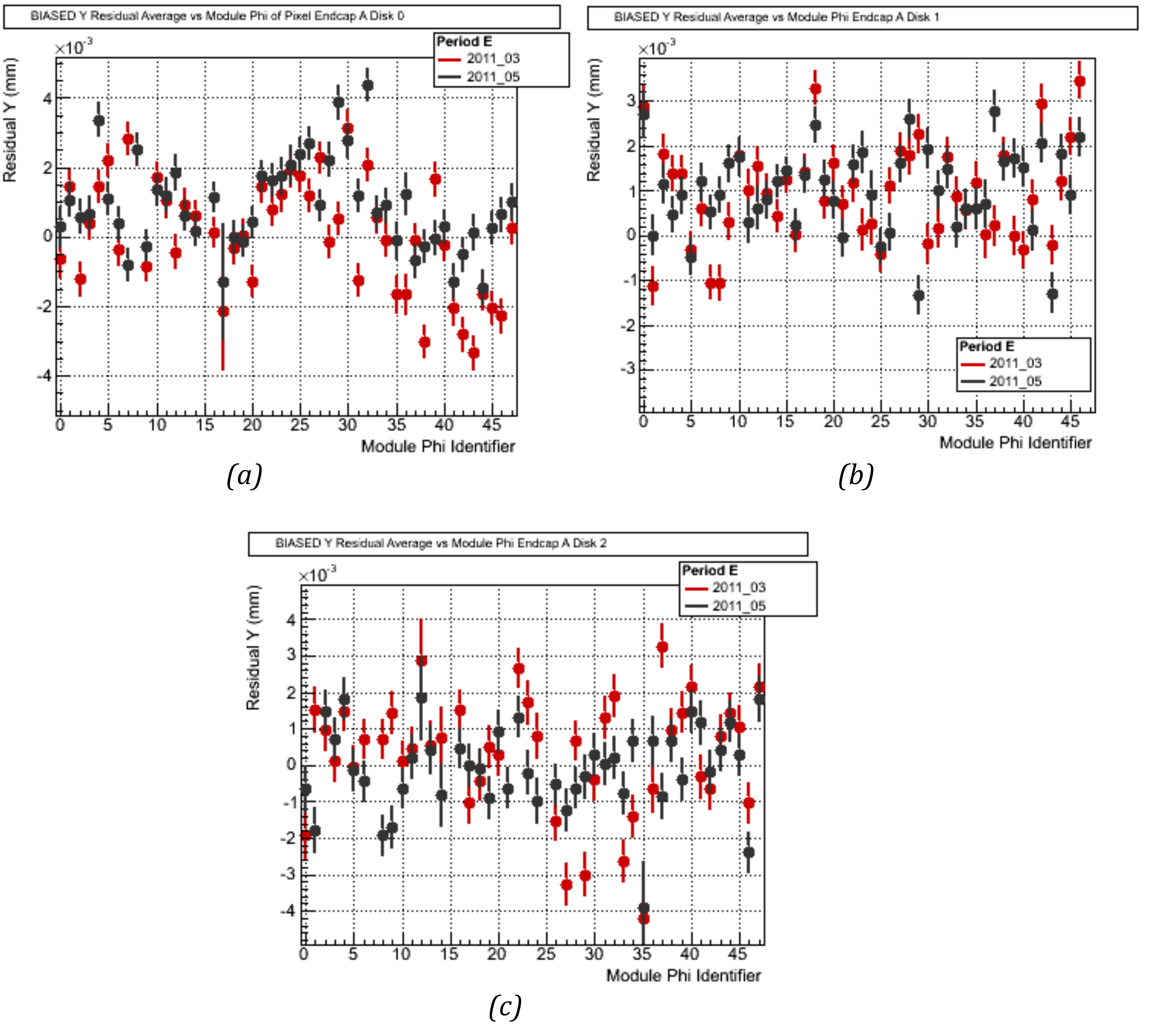

Figure 5.14: *Averaged **biased y** residuals vs. Module Phi Identifier of Pixel **end-cap A** where (a) is disk 0, (b) is disk 1 and (c) is disk 2.*

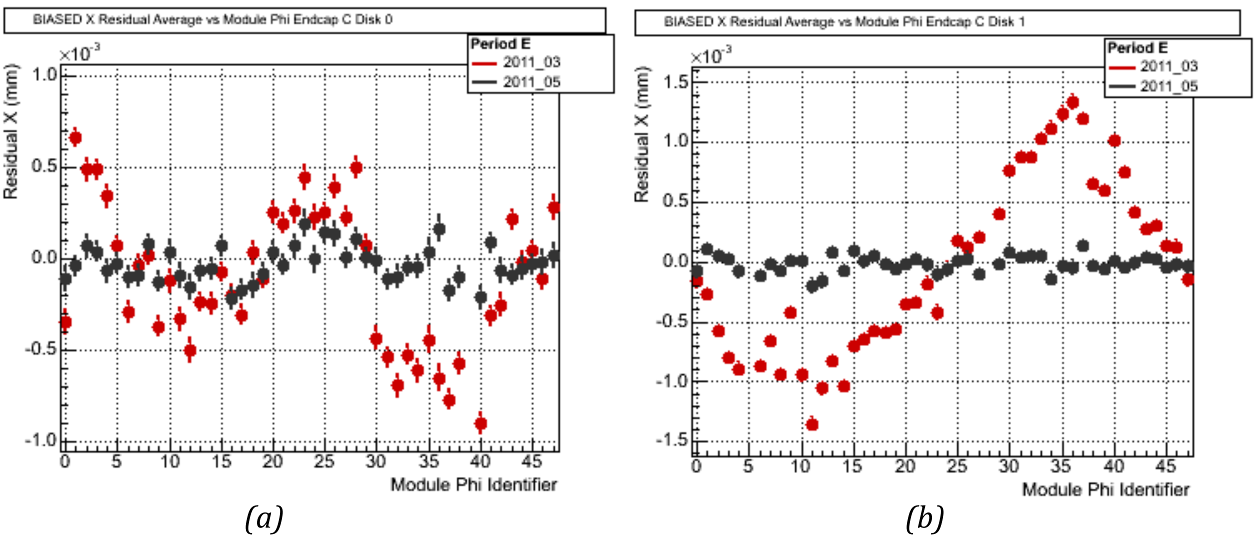

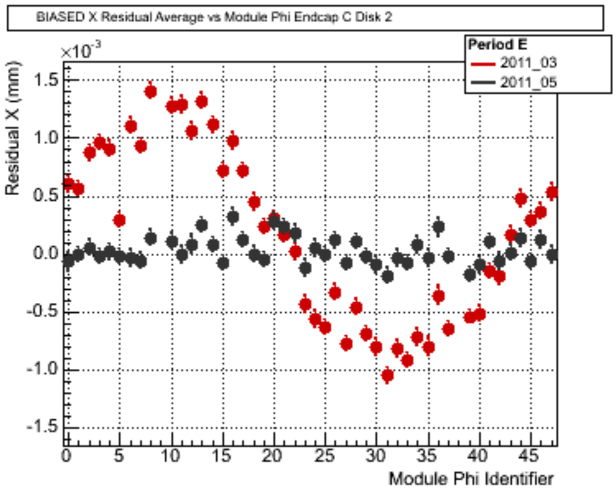

(c)

Figure 5.15: *Averaged* ***biased x*** *residuals vs. Module Phi Identifier of Pixel* ***end-cap C*** *where (a) is disk 0, (b) is disk 1 and (c) is disk 2.*

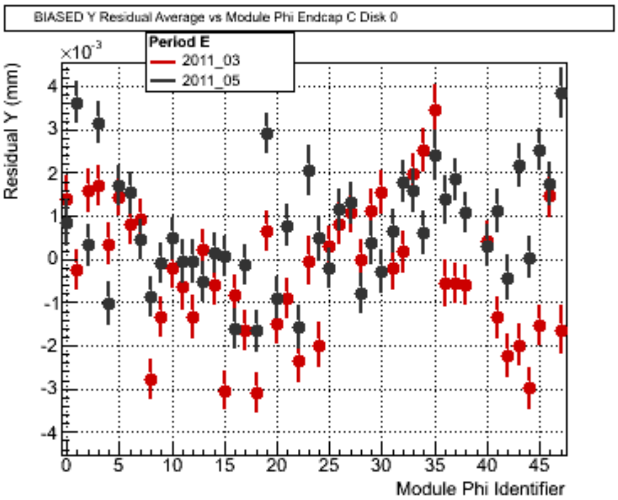

(a)

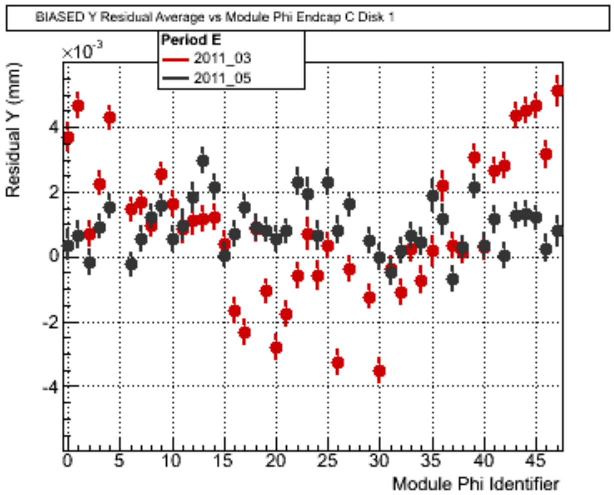

(b)

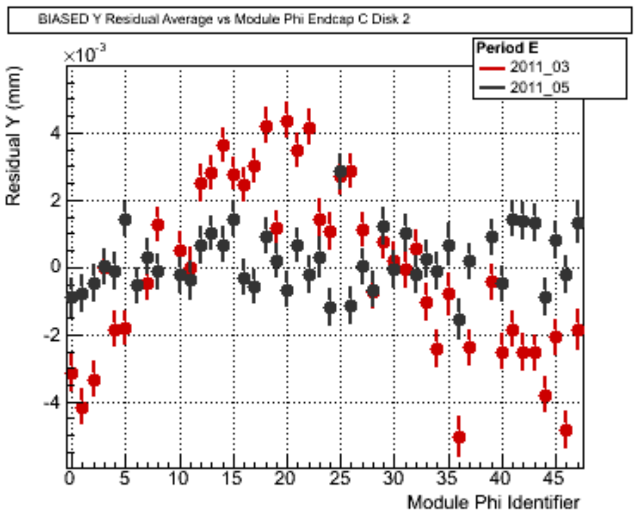

(c)

Figure 5.16: *Averaged* ***biased y*** *residuals vs. Module Phi Identifier of Pixel* ***end-cap C*** *where (a) is disk 0, (b) is disk 1 and (c) is disk 2.*

From all these previous histograms it is evident that the alignment of the ID has been improved with the newest constants (i.e. the ones that give the black lines or dots). That's one of the reasons why these new plots are important, because one can immediately see if the alignment is working properly or not.

The average Unbiased X and Y Residuals vs the Module Phi Identifier of the Pixel end-caps for each disc separately have been added to the ATLAS Data Quality Monitoring (DQM) web page. The DQM is an important and integral part of the data taking process of HEP Experiments. When DQM occurs in the online environment, it provides the shifter with current run information that can be used to detect problems early on. Also, during the offline reconstruction, more complex analysis of physics quantities is performed by DQM, and the results are used to assess the quality of the reconstructed data. The DQM web page has been of great help in providing quick feedback, to all the subsystems in general, about the functioning and performance of the different parts of ATLAS by providing a configurable easy and fast visualization of all the relevant information.

Specifically for the ID alignment, it is the shifters duty to check all the relevant DQM web page histograms, which include those unbiased residuals new ones, to quickly find any possible problem. Therefore, we can conclude that these new histograms are a very important and useful tool for the ID alignment monitoring that will make easier and faster to trace any possible problem.

6 Conclusions

The ATLAS Inner Detector tracking system was aligned using 2010 LHC proton-proton collision data at a centre of mass energy of 7 TeV, as well as cosmic-ray tracks recorded between LHC collisions. The alignment approach used is a track-based algorithm that minimizes a χ^2 based on track-hit residuals. Different alignment levels were defined corresponding to the detector assembly structures. The track statistics were large enough that individual detector elements were aligned: pixel and SCT modules and TRT wires. Moreover, the pixel barrel module distortions were also used.

The use of the 7 TeV collision data allowed the selection of a large sample of high p_T tracks, minimizing the material effects in the tracking and maximizing the sensitivity to the alignment effects.

The results show a large improvement of the alignment precision when compared to the previous alignment (based on 900 GeV collision data). The improvements are evident also in the maps of the residual means, which after the alignment exhibit a significant reduction of the internal structure of the detector components (silicon modules and TRT wires).

The higher statistics of the 2011 data have enabled a run-by-run alignment, leading to a monitoring of the detector movements as a function of time, making visible the correlation between the detector stability and the operation conditions.

Important improvements have also been made in the fight against weak modes, using external constraints such as invariant masses of well known resonant decays or the E/p of electrons.

All the results of the alignment procedure have been validated with different sets of data than the ones used to obtain the alignment constants.

New histograms related with the BS parameters (used as constraints for the alignment) have been added to the ID monitoring software packages with the purpose of having the input for the alignment completely monitored.

Also residual histograms for the Pixel end-caps discs have been added to the monitoring packages and furthermore to the ATLAS DQM web page. These plots are useful for the online monitoring as well as for validation of the data.

The future plans of the Alignment Group are:

- keep fighting against the systematic errors, such as the weak modes (a publication about this topic is expected to be ready in the next few months),
- perform more studies of the detector movements and
- achieve a better description of the modules' internal distortions.

The ID Alignment plays an important role in the ATLAS physics program and, although being very challenging, after several years of hard work, it currently works very well.

References

[1] L. Evans and P. Bryant, LHC Machine, J. Instrum. 3 (2009) S08001.

[2] ATLAS Collaboration, The ATLAS experiment at the CERN Large Hadron Collider, J. Instrum. 3 (2009) S08003.

[3] C. P. Burgess and G.D. Moore, The Standard Model: A Primer, Cambridge University Press (2007).

[4] ATLAS Collaboration, Alignment requirements, in ATLAS Inner Detector Technical Design Report, vol. I, p. 215. CERN_LHCC_1997-016, CERN, Geneva, 1997.

[5] The CMS Collaboration, The CMS experiment at the CERN Large Hadron Collider, J. Instrum. 3 (2008) S08004.

[6] The LHCb Collaboration, The LHCb Detector at the Large Hadron Collider, J. Instrum. 3 (2008) S08005.

[7] The ALICE Collaboration, The ALICE experiment at the CERN Large Hadron Collider, J. Instrum. 3 (2008) S08002.

[8] The TOTEM Collaboration, The TOTEM Experiment at the CERN Large Hadron Collider, J. Instrum. 3 (2008) S08007.

[9] The LHCf Collaboration, The LHCf detector at the CERN Large Hadron Collider, J. Instrum. 3 (2008) S08006.

[10] LHC Computing Grid project website. http://lcg.web.cern.ch.

[11] C. Escobar, Alignment of the ATLAS silicon tracker and measurement of the top quark mass. PhD thesis, Universitat de València, July 2010. CERN-THESIS-2010-092.

[12] H. Härtel, Studies on an initial top quark mass measurement at ATLAS in the lepton+jets top-antitop decay channel and alignment of the Pixel and SCT subdetectors. PhD thesis, TU München, June 2009.

[13] The MoEDAL experiment web site: http:// moedal.web.cern.ch.

[14] ATLAS Collaboration, Alignment of the ATLAS Inner Detector Tracking System with 2010 LHC proton-proton collisions at $\sqrt{s}$ = 7 TeV, ATLAS NOTE, March, 2001. ATLAS-CONF-2011-012.